

DEVELOPMENT OF AN AXIAL YIELDING DEVICE FOR
MASONRY WALLS

Development of an Axial Yielding Energy Dissipation Device for Controlled Rocking Masonry Walls

Written By

DANIEL A. LEE KIM, B.ENG.MGMT.

A Thesis Submitted to the School of Graduate Studies in Partial
Fulfillment
of the Requirements for the Degree of Master of Applied Science



McMaster University

©Copyright by Daniel A. Lee Kim, September 2019

MASTER OF APPLIED SCIENCE (2019)
McMaster University

(Civil Engineering)
Hamilton, Ontario

TITLE: Development of an Axial Yielding
Energy Dissipation Device for
Controlled Rocking Masonry Walls

AUTHOR: Daniel A. Lee Kim, B.Eng.Mgmt
(McMaster University)

SUPERVISORS: Dr. Lydell A. Wiebe
Dr. Mohamed Ezzeldin

NUMBER OF PAGES: x, 92

LAY ABSTRACT

Earthquakes can cause incredible damage to cities specifically to their critical infrastructure systems. The economic effects of such seismic damage can last for a prolonged time due to the inability to repair crucial structures, such as hospitals and schools. The need for easily designable and repairable energy dissipation devices is crucial for all structures, but especially masonry structures due to the lack of current research.

This thesis describes the development, testing, and modelling of a new axial yielding energy dissipation device for controlled rocking masonry walls. The experimental work demonstrated that the new device can achieve an acceptable level of performance through appropriate energy dissipation and force capacities for the intended application. The numerical developed model was shown to be an effective tool for predicting the seismic performance of the device.

ABSTRACT

The damage caused due to a seismic event can leave a city destabilized. However, the negative effects can last much longer because of the inability to reoccupy critical infrastructure systems due to their demolition and eventual rebuild. In order to minimize the recovery time following a seismic event, energy dissipation devices can be installed to absorb the majority of the seismic damage and subsequently maintain the main structure serviceable. One researched solution is by allowing controlled rocking of a masonry wall. A controlled rocking masonry wall uses its own gravity load along with a yielding energy dissipating device as a restoring force to return the wall to its original vertical alignment.

Through iteration, a new axial yielding energy dissipation device was designed in the current study to be installed to a controlled rocking masonry wall. The proposed device was designed to provide the required supplemental energy dissipation, while also being replaceable in the event of seismic damage. The device takes inspiration from structural buckling restrained braces, which includes a yielding steel core, a rubber debonding layer, and a confining grout all within a steel casing. The device is bolted into the wall foundation as well as into a special steel portion of the wall that prevents toe damage and provides a rigid section for the installation of the device. Furthermore, the overall design of the new device maintains the footprint of a standard masonry wall.

After initial conceptual development of an axial yielding device, half-scale testing was performed to assess the seismic performance of nine specimens with different design parameters. Quasi-static uniaxial testing, through adapters on a uniaxial tester, was performed to simulate the actual boundary conditions for the bolted ends of the specimens. Parameters investigated in the current study included the cross-sectional area of the yielding core, the thickness of a rubber debonding layer, and the effective length of the core. An OpenSees model was then developed to simulate the seismic performance of the new device. The model was validated against experimental results and further verified using mechanics to evaluate the maximum force of the device when designed with different geometrical configurations. The results of the study show promise of both a feasible energy dissipation device and an effective tool for estimating performance prior to conducting detailed design.

ACKNOWLEDGEMENTS

In the process of writing this thesis, there was certainly a lot of time that was spent reflecting on the journey that has culminated finally in writing this section. To be honest, it is an incredibly surreal feeling to finally get to this point. But with that being said, it certainly goes without saying that completing a graduate degree is the work of more than just the student...

Thank you to my supervisors, Lydell Wiebe and Mohamed Ezzeldin. Thank you for all of your guidance and support throughout what has been maybe the longest two years of my life. Your standards have always been incredibly high, and reaching for them has been one of the most challenging and rewarding things I've ever done.

To my senior lab mates: Taylor Steele, Paul Steneker, and Ahmed Yassin. You were always there for technical support but more importantly guidance and being a role model. Thank you for showing me how to be a grad student all in your own different ways.

I would like to give a huge thank you to the lab technicians we have at the ADL: Kent Wheeler and Paul Heerema. It really is amazing to see how stir crazy one student can become when every single day is spent testing in a windowless box. But you two made it somewhere that I looked forward to working in every morning.

For my friends, who were there when more than just my thesis was going wrong: Mike Sucharda, Matt East, Ricky Darlington, Mariano Colicchio, Trevor Reade, Alex Dufault, Tom Wille, Neil MacPhee, Ryan Rogers, Taylor de Vet, Kevin McNamara, Jeff Li, and Josh Hoekstra. Thank you for all the little things that made the hard times good, and the good times better.

Finally, I'd like to thank my family. To my dad, I know you were just as uncertain as I was when I first agreed to do a Master's Degree. But you were able to guide me through undergrad since you also have your Iron Ring – and even though you didn't know how to help sometimes, it was always nice to hear some kind of support. Mom, thank you for putting up with every ounce of stress, frustration, and anger that came complementary with this degree and especially for undying support even when I didn't want it. To my brother Christian, you may not realize it, but you also helped, somehow. Thank you for letting me have conversations with you that I could never have with anyone else.

There are so many people that I'm certain are escaping me at this very second, but while I'm reminiscing about this last leg of my academic life, I want to thank everyone that I have had the pleasure to work, plan and organize, lead, teach, and/or spend quality time with during my seven years at McMaster. It will always be a part of me. Thank you.

Contents

1	INTRODUCTION	1
1.1	Motivation	1
1.2	Objectives & Research Approaches	2
2	BACKGROUND & LITERATURE REVIEW	4
2.1	Controlled Rocking	4
2.1.1	Controlled Rocking Masonry Walls	6
2.2	Energy Dissipation Devices	9
2.2.1	Tension-Only Devices	9
2.2.2	Tension-Compression Devices	10
2.2.3	BRB Components	12
2.2.3.1	Debonding Layer of BRBs	12
2.2.3.2	Bracing Material	14
2.2.4	BRBs in Different Applications	16
2.3	Numerical Modelling of Buckling Restrained Braces	21
2.3.1	Finite Element Analysis	22
2.3.2	OpenSees Modelling	25
3	EXPERIMENTAL PROGRAM AND RESULTS	27
3.1	Device Design Motivation and Test Goals	27
3.2	Test Specimen Preliminary Design	29
3.2.1	Steel Restraining Case	30
3.2.2	Steel Yielding Core	30
3.2.3	Rubber Debonding Layer	32
3.2.4	Grout Design and Bracing Strength	33
3.3	Test Instrumentation and Setup	34
3.4	Construction Process	38
3.5	Parametric Study Schedule	44
3.6	Loading Protocol	45
3.7	Coupon Test Results	46
3.8	Test Results	47
3.8.1	Effective Length Specimens	49
3.8.2	Cross-Sectional Area Specimens	51
3.8.3	Rubber Thickness Specimens	53
3.9	Ductility	55
3.10	Energy Dissipation	56

4	NUMERICAL MODELLING	60
4.1	Modelling Approach	60
4.2	OpenSees Model	61
4.2.1	Model Overview	61
4.2.2	Model Validation	63
5	SUMMARY AND CONCLUSIONS	70
5.1	Summary	70
5.2	Conclusions	71
5.3	Recommendations for Future Research	73
6	REFERENCES	75
A	BASE DESIGN CONNECTIONS	79
B	SHIMADZU ADAPTER DESIGN	84
C	APPENDIX REFERENCES	92

List of Figures

2.1	Controlled rocking of a braced steel frame (Steele and Wiebe, 2016)	5
2.2	A post-tensioned masonry wall	6
2.3	Schematic of Laursen's tested walls (2008)	7
2.4	Schematic of Laursen's energy dissipation devices (2008)	8
2.5	Grip n' Grab prototype assembly (Cook et al., 2015)	10
2.6	Common BRB assembly	11
2.7	Debonding layer and clearance post-yield in tension (Tsai et al., 2014)	13
2.8	Schematic of unbonded brace studies conducted by Fujimoto et al. (1990)	16
2.9	Over view of the Shinkawa building (Fujimoto et al., 1990)	17
2.10	Drawing of Toranzo-Dianderas' design (Toranzo-Dianderas, 2002)	19
2.11	Results of Toranzo-Dianderas' cyclic testing (Toranzo-Dianderas, 2002)	20
2.12	Schematic of Sarti's fuse design (2016)	21
2.13	Buckling of Sarti's fuse (2016)	21
2.14	The hysteretic behaviour of a typical BRB (Clark et al., 2000)	22
2.15	Schematic of Shi's all-steel BRB (Shi et al., 2018)	23
2.16	Different parts of Shi's core plate (Shi et al., 2018)	24
2.17	Simplified FEA model used by Rahnavard et al. (2018)	25
3.1	Exploded view of proposed device installation (the first masonry course of the wall is not shown for illustration)	27
3.2	Schematic of the base specimen (Units in mm)	29
3.3	Stress-strain curves of common steel grades (Bruneau, 2011)	31
3.4	Schematic of adapter design	35
3.5	Full assembly of adapter installed into the Shimadzu	35
3.6	String potentiometer installation	36
3.7	Installation of string potentiometers	37
3.8	Full schematic of instrumentation	37
3.9	Custom cut steel yielding core	39
3.10	Confining case assembly before full weld	40
3.11	Preparation for rubber application	41
3.12	Temporary wedges used during grout pouring	42
3.13	Assembling specimens for casting	43
3.14	All specimens being prepared for casting	43
3.15	Planned loading protocol	46
3.16	Coupons test results from both steel orders	47
3.17	Experimental results	49
3.18	VL LONG Specimen: Yielding core after tension half-cycle	50
3.19	Permanent damage of retaining case	51
3.20	3W Specimen: Rubber and grout damage	54
3.21	Comparison of specimen energy dissipation	59
3.22	Comparison of cumulative specimen energy dissipation	59

4.1	Schematic diagram of the OpenSees model	61
4.2	Comparison of steel elastic modulus and device elastic modulus . . .	62
4.3	Steel4 MinMax model compared to VL BASE experimental results . .	64
4.4	Steel4 MinMax model compared to 0W experimental results	67
4.5	Steel4 MinMax model compared to XS23 experimental results	68
A.1	Base connection design	80
A.2	Net section connection fracture	81
A.3	Bolt tear out connection fracture	82
A.4	Bolt bearing connection fracture	83
B.1	Adapter connections	85
B.2	Adapter net fracture	86
B.3	Adapter bolt tear out	87
B.4	Adapter bolt bearing failure	88

List of Tables

3.1	Planned test schedule	44
3.2	Specimen ductility results	56
3.3	Specimen energy dissipation results	57
4.1	Steel4 Parameters	66
4.2	MinMax Parameters	66
4.3	Comparison between OpenSees model and experimental results	69

1 INTRODUCTION

1.1 Motivation

The destructive power of earthquakes can destabilize countries for significant periods of time, if they reside near tectonic plate boundaries. For example, Mexico experienced multiple earthquakes in 2017, including the strongest ground motion in a century. About 1.85 million homes were left without power, with 25% powerless and without water services for up to 48 hours (Berlinger et al., 2017). In addition to the damage associated with critical infrastructure, the cost of repairs to residential and commercial buildings often makes it more economical to demolish (Iwata et al., 2005). Consequently, there is still a need for effective seismic force resisting systems that provide both minimal structural damage and downtime after seismic events.

To achieve this goal, the implementation of a controlled rocking frame (Wiebe, 2013) has shown to be an effective method of mitigating structural damage. Often used with steel structures, the notion of controlled rocking can also be applied to masonry structures that remain prevalent all over the world (Laursen, 2004; Hassanli et al., 2017a). More specifically, the use of masonry is still common in the developed world, including Canada, for high-importance buildings (e.g. schools and hospitals) because of its durability. However, due to toe crushing, standard masonry construction is inherently more susceptible to significant damage at the base of a structure

when controlled rocking is implemented (Priestley and Elder, 1983).

This project is part of a multi-phase research program that was initiated at McMaster University to develop controlled rocking masonry walls with an enhanced seismic performance compared to that of conventional masonry walls with fixed base. The thesis is expected to provide effective and efficient seismic protection throughout conventional construction as required.

1.2 Objectives & Research Approaches

This research will establish an economical and effective energy dissipation device that allows for controlled rocking of structural masonry walls. The energy dissipation device established by this research project is expected to improve accessibility and reparability, thus reducing post-disaster costs. The objective of this research is to develop and assess the seismic performance of an axial yielding device that can:

- Provide a high energy dissipation capacity.
- Demonstrate that target forces and displacements can be consistently achieved.
- Be easily replaced.
- Be installed without impacting the footprint of the wall.

The steps to accomplish this objective can be summarized as:

1. Develop a design concept for an axial yielding device that accommodates the constraints associated with masonry structures. (**Chapter 2**)
2. Design the individual components of the device in order to withstand the target displacement. (**Chapter 3**)
3. Design the axial yielding device to the desired specifications according to CISC S-16 standards. (**Chapter 3**)
4. Design a test matrix and perform experimental tests according to FEMA 461 (FEMA, 2007) loading protocol. (**Chapter 3**)
5. Develop an OpenSees (OpenSees, 2016) numerical model to experimental results. (**Chapter 4**)
6. Provide a summary of the research and provide conclusions that can be used to further advance the objectives of this project. (**Chapter 5**)

2 BACKGROUND & LITERATURE REVIEW

This section summarizes the previous research that was deemed relevant to this project. In Section 2.1, a deeper understanding of a controlled rocking mechanism was explored which then led to the investigation of controlled rocking in steel frames and how that differs from masonry walls. Energy dissipation devices were then investigated in Section 2.2 to find inspiration for the design of the device developed in the current study. Buckling restrained braces (BRBs) were found to be the most attractive option, and therefore, a deeper investigation of current design requirements was presented. Finally, Section 2.3 provides different approaches of numerical modelling presented in previous research studies for BRB devices.

2.1 Controlled Rocking

Serviceability is an important requirement when a structure is being designed against seismic events. Previous research studies have suggested that 0.5% of residual drift can be enough to make rebuild of infrastructure systems a more economical solution over repair (McCormick et al., 2008). Controlled rocking seismic systems serve as a self-centering alternative to conventional seismic systems (with a fixed base) that requires energy to be dissipated through plastic yielding of some components of a structure. A self-centering structure has a restoring force that allows such a structure to return to its original vertical alignment after experiencing a seismic event. There-

fore, controlled rocking seismic force resisting systems have become a very attractive option for high importance or post-disaster rated buildings and structures.

Research has been conducted on controlled rocking with various materials including steel (Wiebe, 2013), wood (Kovacs, 2016), and concrete (Toranzo-Dianderas, 2002; Laursen, 2008; Sarti et al., 2016). Shown by Steele and Wiebe (2016) in Figure 2.1, a flag-shaped hysteresis is created during the controlled rocking of a steel frame. Figure 2.1 shows that the initial stiffness of this frame is provided by the steel frame, with applied energy dissipation devices holding it down. Once the devices have slipped or yielded in tension at the corners of the steel frame, a second stiffness is provided by post-tensioning elements in the frame. During unloading, the initial stiffness is once again provided by the frame before returning to its original vertical alignment, thus minimizing residual displacements due to damage.

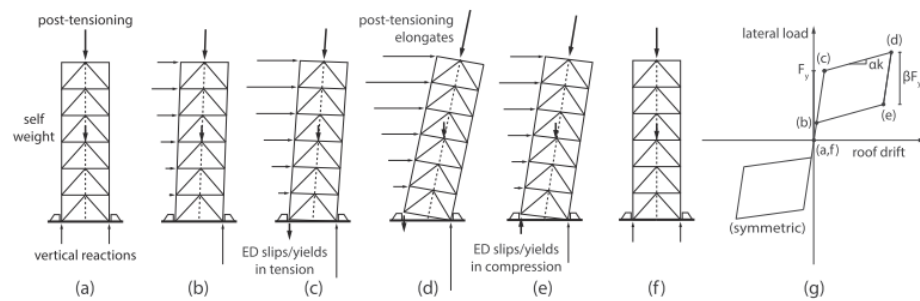


Figure 2.1: Controlled rocking of a braced steel frame (Steele and Wiebe, 2016)

2.1.1 Controlled Rocking Masonry Walls

For masonry walls, the term “rocking” has typically been associated with the flexural failure mode in both reinforced and unreinforced scenarios (Rosenboom and Kowalsky, 2004). During cyclic loading, walls experience extensive damage at their compression toes. A negative feedback loop is created, as more degradation encourages further rocking. In contrast, controlled rocking masonry walls (CRMWs) designed in the current study allow the structure to vertically displace in a rocking mode prior to any cracks induced by a flexural mode.

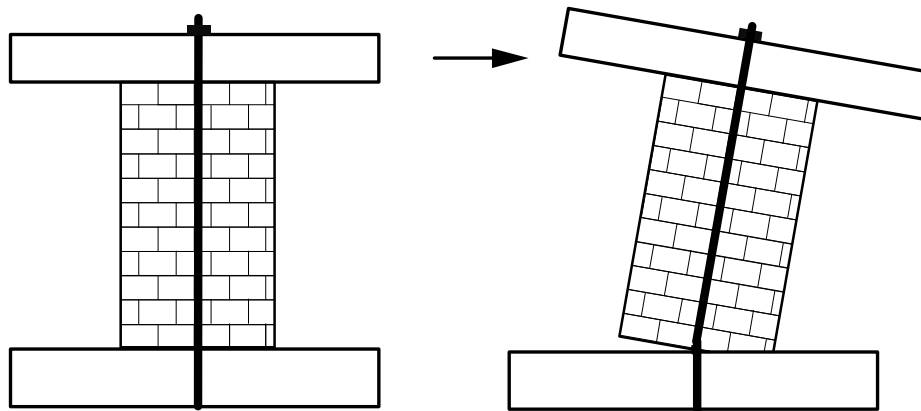


Figure 2.2: A post-tensioned masonry wall

Relevant research has been mainly conducted on post-tensioned masonry walls shown in Figure 2.2, where self-centering capabilities are typically achieved by post-tensioning tendons to apply restoring forces. For example, Laursen and Ingham (2001) investigated single-story post-tensioned masonry walls constructed of unconfined masonry. These walls were found to have a reliable drift capacity up to 1%. The same authors also demonstrated that strengthening the flexural compression zones with

high compressive strength masonry and additional energy dissipation can improve the drift capacity and delay the onset of strength degradation compared to those of previous walls. The energy dissipation devices installed in these walls were embedded cylindrical steel bars, as shown in Figures 2.3 and 2.4.

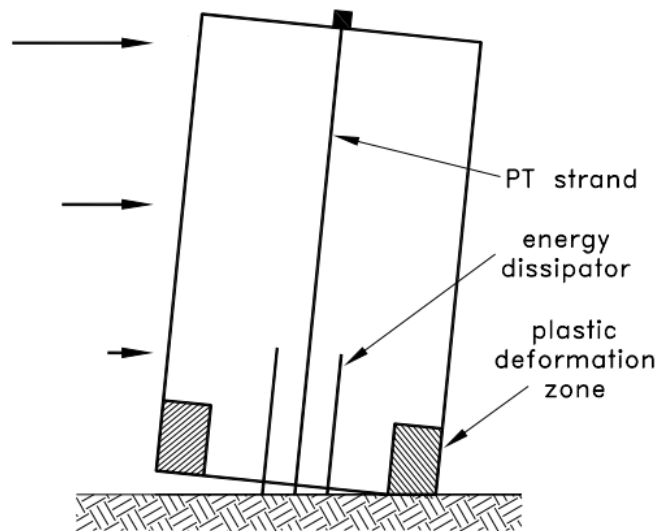


Figure 2.3: Schematic of Laursen's tested walls (2008)

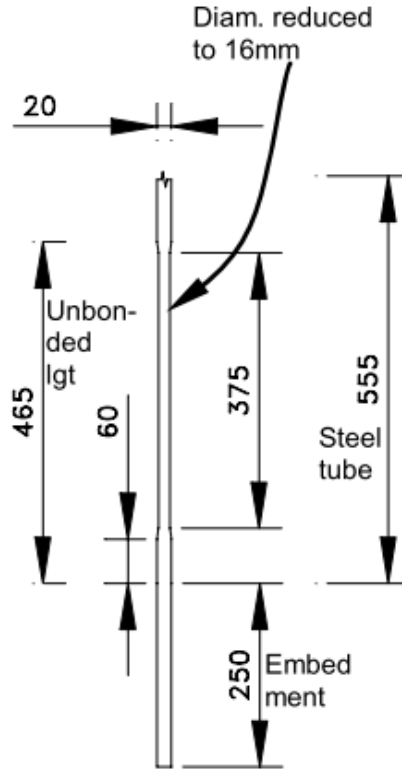


Figure 2.4: Schematic of Laursen's energy dissipation devices (2008)

Hassanli et al. (2017a) also performed a parametric study on unbonded post-tensioned masonry walls to develop a design procedure to predict the in-plane flexural strength of the walls. Experimental results and a finite element analysis (FEA) model were used to determine the accuracy of the design procedure. The study recommended that the axial stress ratio (e.g. defined as the ratio between the axial stress in the post-tensioning tendons and the compressive strength of the wall) should be limited to 15%. Hassanli et al. (2017b) later developed a simplified approach that can predict the wall flexural strength within 10% of the actual strength of the wall as long as the axial stress ratio of the wall was less than 20%. It was also shown that

ignoring the elongation of the post-tensioning bar in strength prediction resulted in an underestimation of 40% (Hassanli et al., 2017a).

While this previous research has generally shown effective ways of self-centering behaviour, having the steel energy dissipation devices embedded in the walls makes it difficult or impossible to repair after an earthquake event.

2.2 Energy Dissipation Devices

2.2.1 Tension-Only Devices

Previous research studies have been conducted on tension-only devices to show their performance when adopted within different seismic force resisting systems. For example, Cook et al. (2015) designed a functional prototype of what was coined a Grip n' Grab device. The device used a slender steel fuse that would yield in tension while engaging into a rack to feed the yielding fuse into the main body during compressive cycles. An exploded view of the prototype is shown in Figure 2.5. Since compressive buckling was not a concern, the device was able to mitigate the associated residual compressive stresses. However, although a tension-only device performed well in tension during loading, the slack in the system that developed over time was an issue especially around zero displacement.

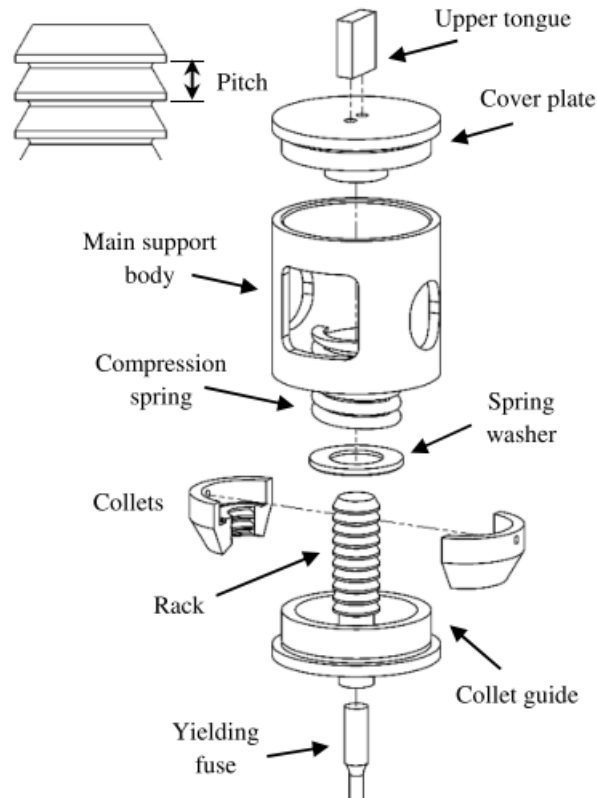


Figure 2.5: Grip n' Grab prototype assembly (Cook et al., 2015)

2.2.2 Tension-Compression Devices

BRBs are tension-compression axially-yielding devices that have multiple layers in order to allow the core material to yield in tension while also being able to withstand nearly equal force in compression. The design of BRBs was initially developed in Japan in the late 1980s and has steadily increased in usage. Since the 1995 Kobe earthquake, Japan began to implement BRBs more frequently in critical infrastructure (Clark et al., 2000). These practices are now part of the CISC S-16 standards when constructing buckling restrained braced frames (BRBF), as shown in Figure 2.6. The typical components of a BRB are a yielding core, debonding layer, concrete or mortar,

and a case. In order to achieve comparable tensile and compressive capacities, the yielding core, typically made from steel, is encased in an assembly that prevents lateral and local buckling in compression. This forces the yielding core to buckle at a much higher load, causing the inelastic capacity of the device to be increased greatly (Tsai et al., 2014).

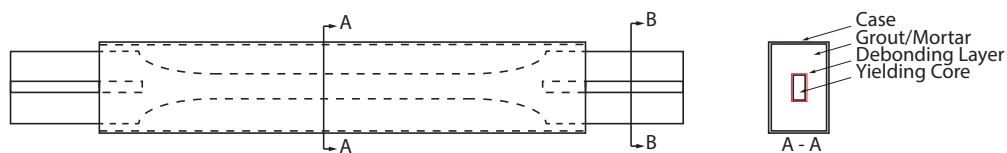


Figure 2.6: Common BRB assembly

BRBs provide excellent energy dissipation characteristics, resulting in a stable and nearly symmetric hysteresis when the cross section has fully yielded. A key advantage of BRBs is that since the buckling of the yielding core is restrained, there should be no degradation during compression cycles (Takeuchi and Wada, 2017).

The first known research reports about BRBs began with Takeda et al. (1972). Tests were performed to increase the buckling capacity of wide-flange sections by encasing them in reinforced concrete. Since a debonding layer was not implemented, the lateral forces provided by a higher mode of buckling caused eventual global buckling. After further iterations, the first project that contained an application of the BRB – known at the time as an unbonded brace for utilizing a debonding layer — was installed for 10 and 15-story steel frame buildings (Fujimoto et al., 1990). The use of this lateral force resisting system began to grow, leading to the inclusion of BRBs in

the Architectural Institute of Japan's (AIJ) design guidelines in 1996 (Takeuchi, 2018).

Since then, various types of BRBs have been designed, where the most common types use a rectangular or cruciform shaped steel yielding core. The performance of BRBs offers significant benefits such as being able to exceed cumulative cyclic inelastic deformations 300 times the initial yield deformation of the yielding core before failure (Sabelli et al., 2003). Currently, there are two main types of BRBs that are typically fabricated. The first is the aforementioned type of BRB that utilizes a debonding layer in combination with a bracing material such as mortar or concrete. The second less common, but widely studied, is manufactured as an all-steel construction, where the yielding core is wrapped in a debonding layer but is braced by a full steel construction. (e.g. Usami et al., 2012)

2.2.3 BRB Components

The following subsections contain relevant research that has been concluded on the individual components of a typical BRB shown earlier in Figure 2.6.

2.2.3.1 Debonding Layer of BRBs

Regardless of the type of BRB, a crucial component in the assembly is the debonding layer. Typically, the debonding layer is a very thin material that is adhesively applied to the yielding core. When designed appropriately, the applied layer allows for a relative movement between the steel and concrete or mortar due to shear forces and

Poisson's effect (Clark et al., 2000). The thickness must be designed in relation to the design forces of the BRB. When the device is subjected to a tension force that causes the steel to start yielding, the steel core thickness, t_c , decreases by $0.5\epsilon_c t_c$ due to Poisson's effect (Tsai et al., 2014), where ϵ_c is the maximum allowable strain of the steel and a Poisson's Ratio of 0.5 for assuming the steel core is incompressible. As can be seen in Figure 2.7, during compression, the newly created gap is split in half during the higher buckling mode.

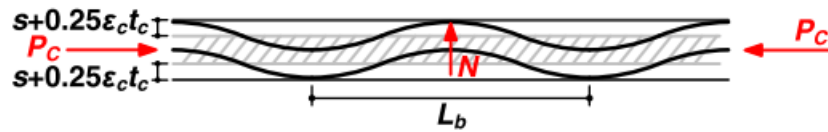


Figure 2.7: Debonding layer and clearance post-yield in tension (Tsai et al., 2014)

Tsai et al. (2014) later provided detail on the optimal debonding material. In their investigation, four different debonding materials were tested: high-density Styrofoam sheet, chloroprene rubber, rubber sheet, and silicone rubber sheet. Results showed that chloroprene rubber provided excellent performance; not only was the compound very effective in minimizing the difference between cyclic peak compressive and tensile strengths, but it was also the most cost-effective option, thus reducing the overall construction cost of the debonding layers by about 50% compared to the other three tested compounds.

2.2.3.2 Bracing Material

The bracing material, typically mortar or concrete, should also be designed to work effectively with the yielding core and debonding material. Since the bracing material causes the core to buckle at a higher mode, there are multiple points of lateral contact with the bracing material that should be resisted. According to Lin et al. (2016), the lateral force of the yielding core against the bracing material, P_b , can be found as:

$$P_b = \frac{4P_{maximum}(2s + \nu\epsilon_{maximum}t_c)}{L_w} \quad (1)$$

$$P_{maximum} = \beta R_y \omega_y \sigma_y A_c \quad (2)$$

$$L_w = \sqrt{\frac{4\pi^2(EI)_{eff}}{P_y}} \quad (3)$$

where $P_{maximum}$ is the maximum force experienced by the device, s is the debonding layer thickness, ν is Poisson's Ratio, $\epsilon_{maximum}$ is the maximum allowable strain, t_c is the thickness of the steel core, L_w is the higher mode wavelength, A_c and σ_y represent the cross-sectional area and yield stress of the yielding core respectively, ω_y and R_y denote the material strain hardening and overstrength factors respectively, $(EI)_{eff}$ is the effective modulus of elasticity times the second moment of area of the core, P_y is the axial yield force, and β corresponds to the compression strength adjustment

factor, which can be found in CISC S-16 (CSA, 2014b) for Canadian construction. According to Lin et al. (2016), EI_{eff} can be calculated as $0.055EI$. Alternatively, instead of using Equation 3, Lin et al. (2016) suggested that the higher mode buckling wavelength, L_w , can be approximately calculated as nine or ten times the steel core thickness for A572 GR50 or A36 steels, respectively.

In order to determine the capacity of the device, Takeuchi and Wada (2017) proposed the Demand Capacity Ratio (DCR_{wh}) as:

$$DCR_{wh} = \frac{B_r - b'}{(2B_r - b' + 2t_m)t_r^2\sigma_{ry}} \frac{4P_{maximum}(2s + \nu\epsilon_{maximum}t_c)}{L_w}, b' \leq 0.85B_r \quad (4)$$

where B_r is the steel case width, σ_{ry} is the yield strength of the restrainer tube material, t_m is the thickness of the bracing material, and t_r is the thickness of the steel case. A DCR less than 1.0 shows that the design yields a greater capacity than the expected lateral force P_b .

The lateral force, P_b , is not necessarily applied as a point load on the grout. According to Takeuchi and Wada (2017), it is suggested that the grout compressive strength, f'_c , should be designed as:

$$\frac{P_b}{t_c B_c} < f'_c \quad (5)$$

where B_c is the width of the steel yielding core.

2.2.4 BRBs in Different Applications

BRBs have been used as hysteretic dampers in buildings of different heights to enhance their seismic performance (Fujimoto et al., 1990; Clark et al., 2000; Toranzo-Dianderas, 2002; Marriott et al., 2009; Sarti et al., 2016). Fujimoto et al. (1990) were the first to design and implement the unbonded brace in the full-scale construction of the 15 storey Shinkawa Building in Chou-ku, Tokyo, as shown in Figures 2.8 and 2.9.

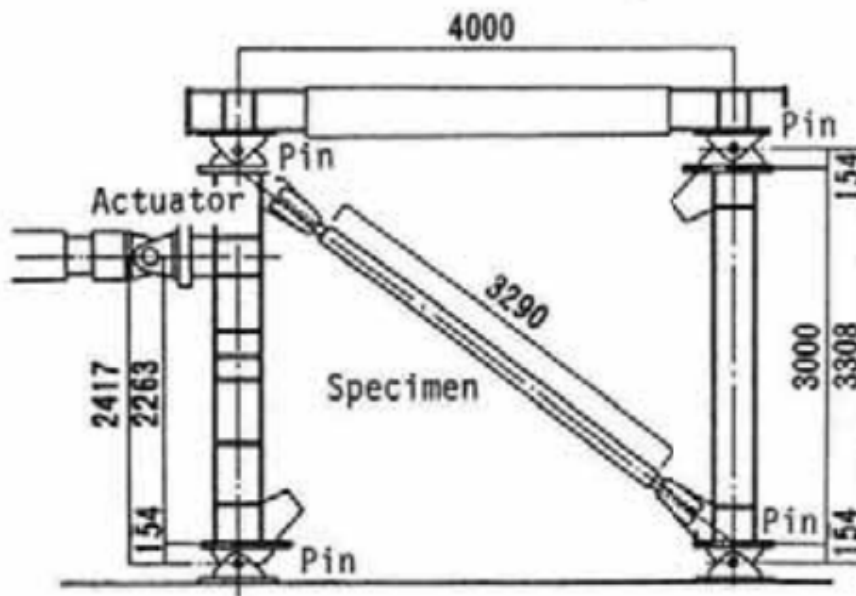


Figure 2.8: Schematic of unbonded brace studies conducted by Fujimoto et al. (1990)

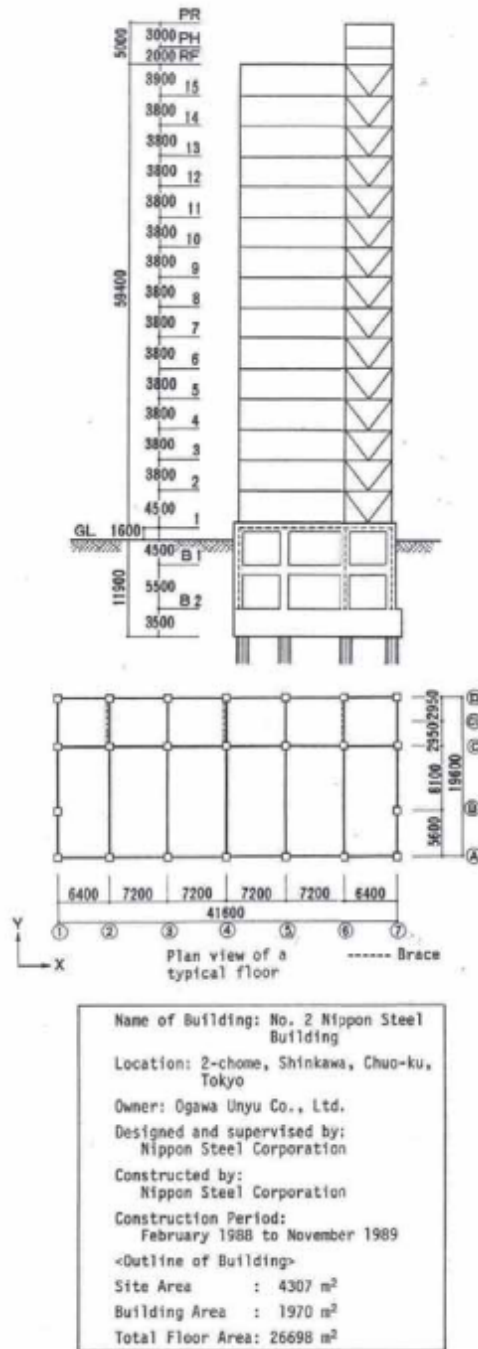


Figure 2.9: Over view of the Shinkawa building (Fujimoto et al., 1990)

Clark et al. (2000) proposed design procedures for steel unbonded braces based on the equivalent static force method. Using this method, a three story model was devel-

oped for nonlinear time history analyses followed by large-scale experimental testing. The time history analyses demonstrated that unbonded brace frames performed better than steel moment resisting frames when interstory drift and base shear were evaluated, while the large-scale tests showed that the proposed design provided predictable behaviour and "substantial overstrength" in terms of displacement and energy dissipation capacities.

Toranzo-Dianderas (2002) briefly explored the idea of using smaller BRBs as an energy dissipator that was attached to a foundation beam surrounding a masonry wall. This device was slightly different from a typical design, as only three sides were covered by a mortar restraining material, with the fourth side lying flush on a plate of steel, as shown in Figure 2.10.

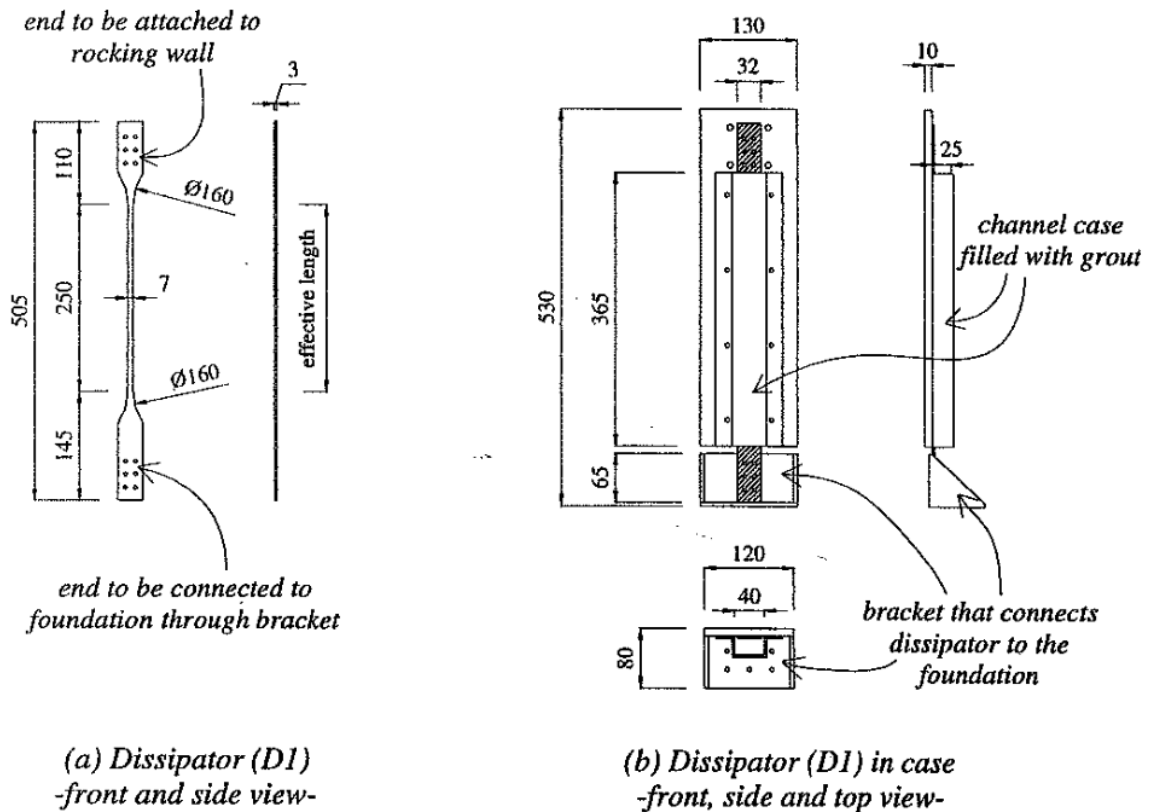


Figure 2.10: Drawing of Toranzo-Dianderas' design (Toranzo-Dianderas, 2002)

In terms of constructability with the design of the wall planned for the current study, Toranzo-Dianderas' design could be easily integrated into the wall; however, the steel plate caused the yielding core to engage the grout as the core buckled. Local buckling resulted in “waves” in the performance of the device, seen in Figure 2.11 as the device began to fail. The steel plate as well as the absence of a debonding layer were two main factors as to why the device was unsuccessful. No further related studies were performed on the device after these tests.

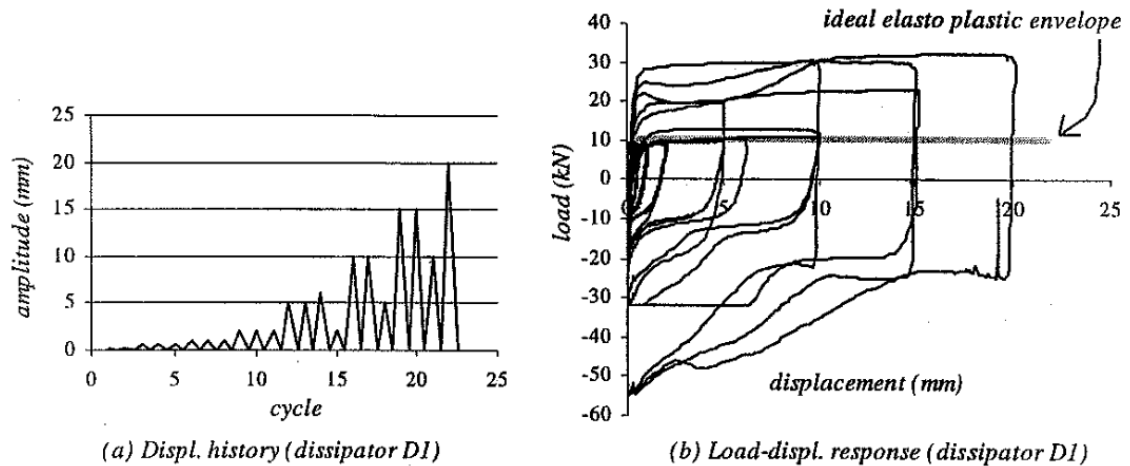


Figure 2.11: Results of Toranzo-Dianderas' cyclic testing (Toranzo-Dianderas, 2002)

Marriott et al. (2009) also tested a device that takes elements of BRBs to dissipate additional energy from bridge piers. Although for a different application, the attractive novelty of the energy dissipators was the idea of low-cost and fully replaceable mild steel yielding dissipaters that were fabricated in-lab. The dissipaters performed well, providing stable response; however, the installation of the devices increased the footprint of the bridge piers. The bridge piers that the dissipaters were installed to still used post-tensioned steel as well.

Sarti et al. (2016) provided lots of insight on devices of this scale. Sarti's device was attached to the corners of a concrete rocking wall and was tested in a parametric study followed by a numerical validation. Figure 2.12 shows the fuse itself was designed as a tapered cylindrical steel bar and encased by a steel confining tube with grout or epoxy inside. However, while the design was intended to prevent the device from buckling

in its first mode, testing showed that this was not the case as shown in Figure 2.13.

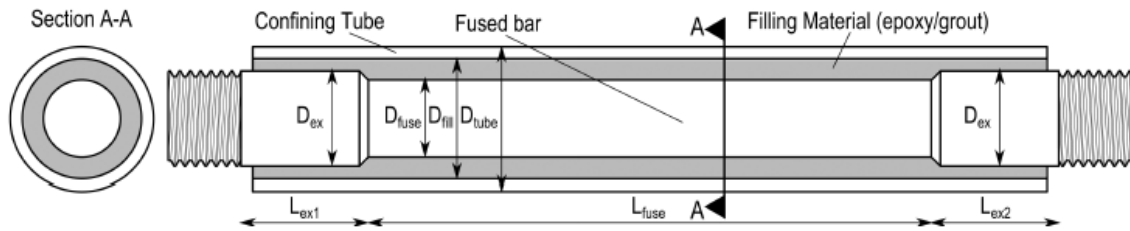


Figure 2.12: Schematic of Sarti's fuse design (2016)



Figure 2.13: Buckling of Sarti's fuse (2016)

2.3 Numerical Modelling of Buckling Restrained Braces

This subsection briefly presents research that has simulated the seismic performance of BRBs using computationally expensive tools such as FEA, and then provides relevant research for modelling using OpenSees. The research in this area is relevant to simulating the hysteretic behaviour of a typical BRB, as shown in Figure 2.14.

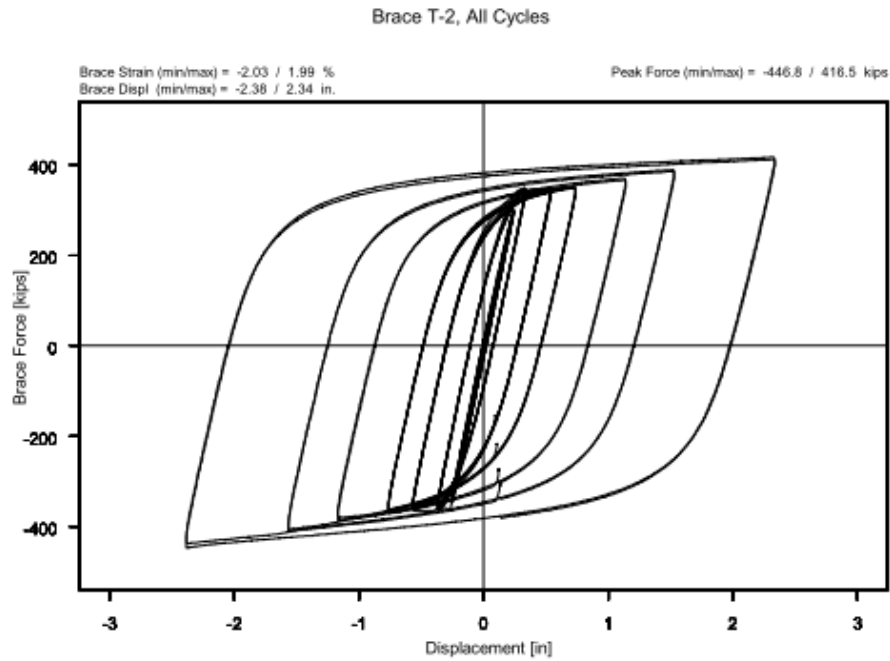


Figure 2.14: The hysteretic behaviour of a typical BRB (Clark et al., 2000)

2.3.1 Finite Element Analysis

The hysteretic behaviour of BRBs along with their corresponding characteristics have been simulated using various software packages by different researchers. Due to the presence of multiple components in a typical BRB assembly, it can be challenging to determine the initial stiffness of the system. When modelling steel-braced BRBs shown in Figure 2.15, Shi et al. (2018) calculated the initial stiffness, K_{tc} , as:

$$K_{tc} = \frac{1}{\left(\frac{1}{K_1} + \frac{1}{K_2} + \frac{1}{K_3}\right)} \quad (6)$$

where K_1 , K_2 , and K_3 are the stiffnesses of the yield, transition, and connecting parts of the core plate, respectively, as shown in Figure 2.16. The secondary stiffness of the

device was defined as a ratio between the yield stiffness and the initial stiffness. After developing this relationship, Shi et al. (2018) later used these two parameters along with other already known variables to model the brace with FEA.

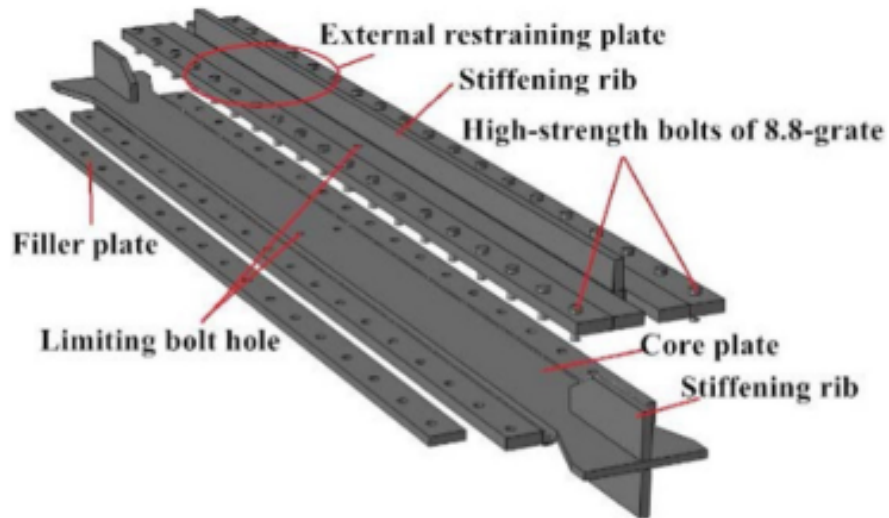


Figure 2.15: Schematic of Shi's all-steel BRB (Shi et al., 2018)

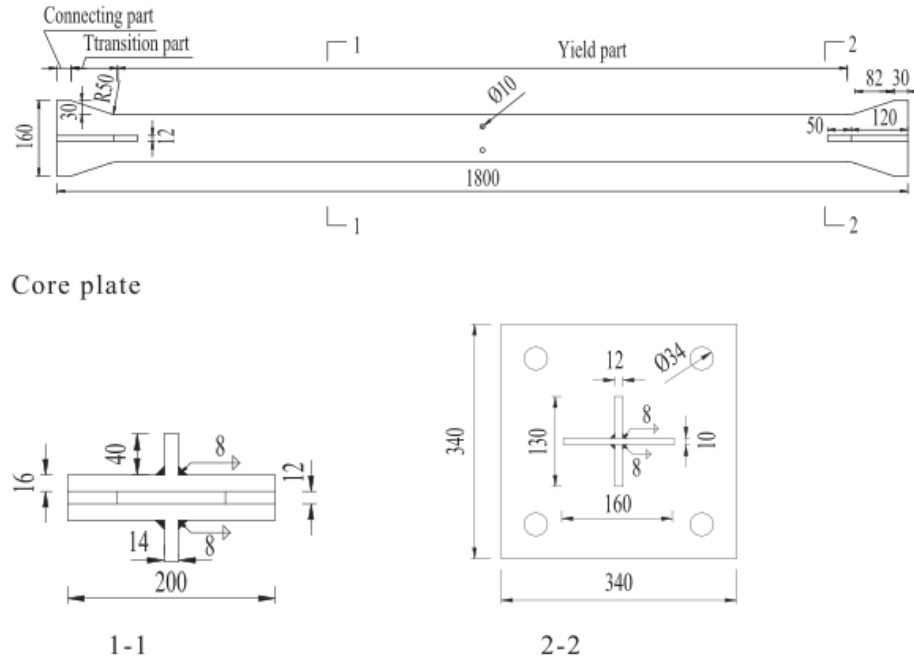


Figure 2.16: Different parts of Shi's core plate (Shi et al., 2018)

Rahnavard et al. (2018) used ABAQUS to model both concentrically braced frames (CBFs) and BRBFs. Rather than attempting to model the complex interaction between the debonding layer, concrete-filled casing, and yielding core, a simplified core-spring model was used. A four-node shell element (S4R) was used in the simplified model as shown in Figure 2.17, where non-linear spring elements were used instead of multiple layers. The model was able to simulate the possible buckling of the core since the deformation capacity was quite large.

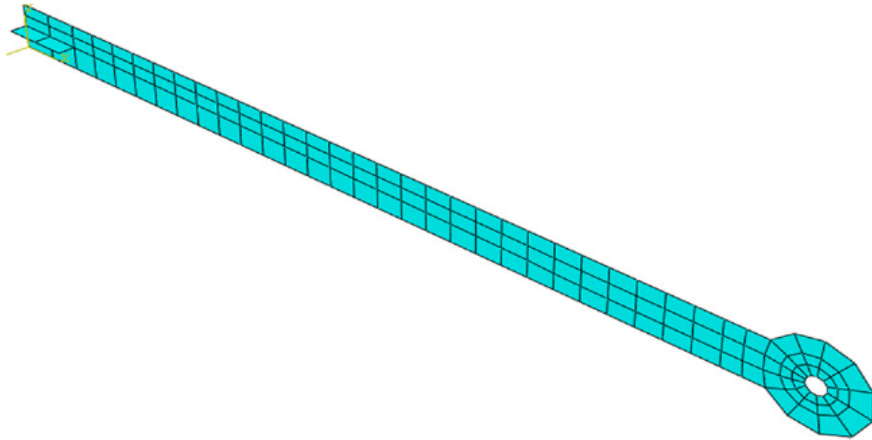


Figure 2.17: Simplified FEA model used by Rahnavard et al. (2018)

2.3.2 OpenSees Modelling

Due to the complex nature of a BRB, the experimental force-displacement hysteresis may need to be simplified. The interaction between the multiple layers of a BRB adds to the parameters that must be considered. As mentioned earlier, FEA models can provide a simplified representation of the device. However, at a global system-level (e.g. a building), more efficient solutions with an acceptable computational time and less numerical convergence issues are still needed.

The OpenSees (2016) Steel02 material has been used frequently in BRB modelling (Zsarnóczy, 2013). Steel02 is based on the uniaxial steel model developed by Menegotto and Pinto (1973), with modifications to the isotropic hardening effect presented by Filippou et al. (1983). The OpenSees material allows users to modify the bilinear behaviour of the element by defining a yield strength, elastic stiffness, and multiple

isotropic hardening parameters (Filippou et al., 1983). Making further changes to this model, Zsarnóczay (2013) developed and tested a steel model now referred to as Steel4 in OpenSees, which is based upon Filippou's model but also allows for kinematic hardening, ultimate strength limits, asymmetrical behaviour, and load history memory. The additional features of Steel4 allow for more control over the shape of the hysteresis, thus allowing users to obtain a more accurate representation of experimental results. Certain features, namely the load history memory, not only reduces the computational effort of the model, but also minimizes certain convergence issues by forcing the kinematic hardening component of the response to converge to the previous load cycles.

3 EXPERIMENTAL PROGRAM AND RESULTS

3.1 Device Design Motivation and Test Goals

In pursuit of developing an axial yielding device, the current research has moved toward utilizing a controlled rocking masonry wall (CRMW) with a steel component connected at the base of the wall. The installation of the steel component maintains the footprint of the wall, while cosmetic fire-proofing face shells make the installed devices not visible. This steel component allows the base of the wall to rock as a rigid mass and also provides a surface to install an energy dissipation device between the wall and its foundation, as shown in Figure 3.1.

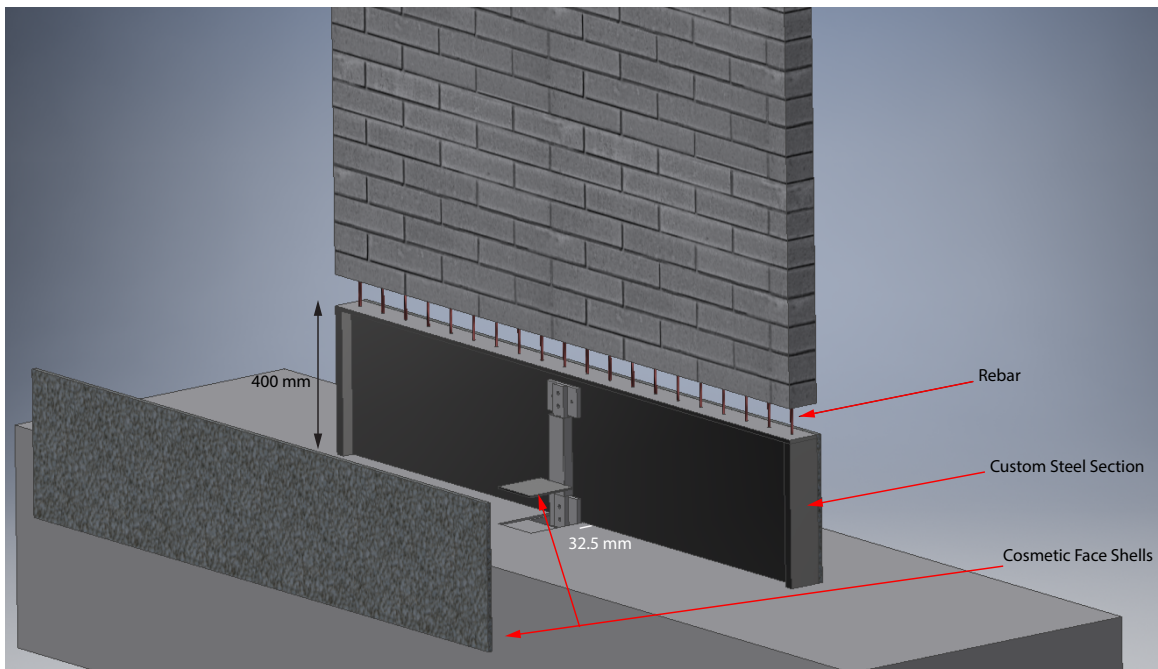


Figure 3.1: Exploded view of proposed device installation (the first masonry course of the wall is not shown for illustration)

The design of the device takes inspiration from BRBs with a smaller scale, similar to the design by Sarti et al. (2016). After a discussion with a member within Dr. Wiebe's research group (Yassin, 2018) at McMaster University, the half-scale walls to be tested in the next phase of this research program are expected to have a maximum force at the corner of the wall of 90 kN corresponding to a maximum corner uplift of 47 mm at 2% wall drift. The device is designed to be placed at the center of the steel component to minimize its displacement requirements to 23.5 mm. The wall is expected to be designed with four devices, reducing the force demand to 45 kN per device.

3.2 Test Specimen Preliminary Design

This subsection presents the primary design calculations used in order to develop the base specimen of the parametric study, as shown in Figure 3.2. Details about the connections and Shimadzu adapter can be found in Appendix A.

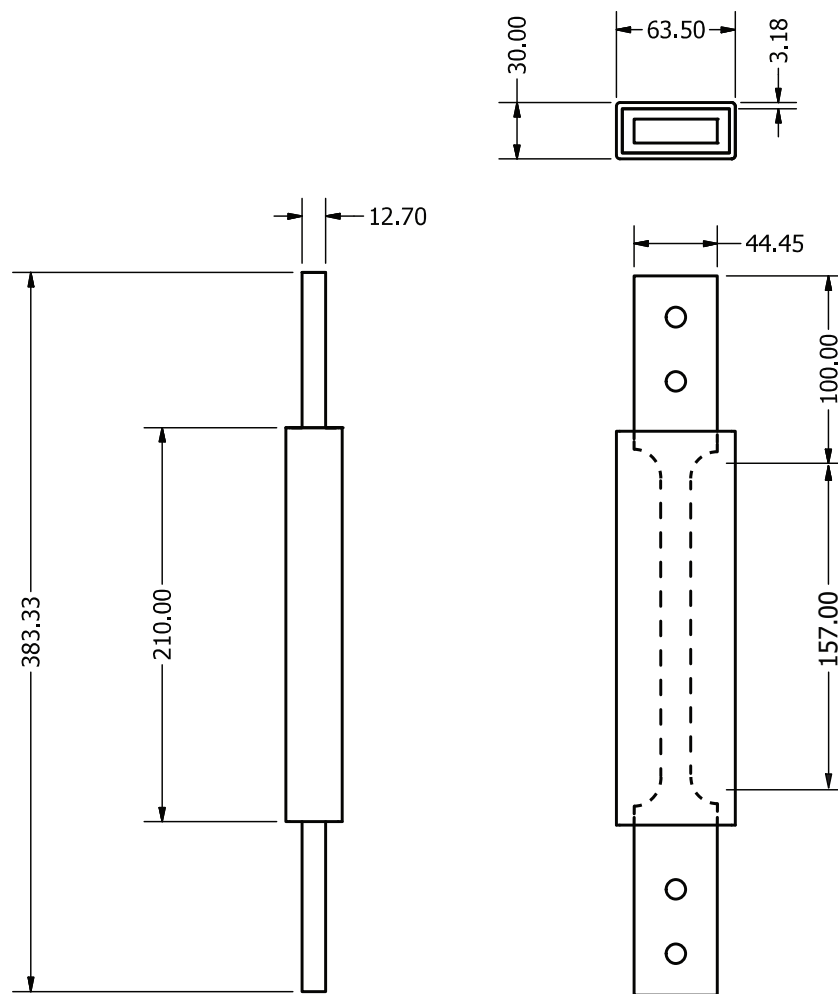


Figure 3.2: Schematic of the base specimen (Units in mm)

3.2.1 Steel Restraining Case

The case is designed to accommodate the size constraints in order to fit the axial device in the steel component of a CRMW, as shown in Figure 3.1. The case is constructed from 3.18 mm [1/8"] thick mild steel that was hand welded in lab, as will be shown later in Section 3.4. The case fully covers the tapered effective length of the device in addition to 20 mm of the head of the yielding core.

3.2.2 Steel Yielding Core

Since the device is a purely axial, the design parameters can be determined mostly using mechanics. The yielding core can be designed to yield at a target force, P , as presented in Equation 7:

$$\sigma = \frac{P}{A} \quad (7)$$

The wall is designed to have one device on each side. This allows for a target yield force of 45 kN, representing half the 90 kN force demands mentioned earlier. 260W steel (CSA, 2014b) was selected for the yielding core for its low yield strength and high strain capacity. The area of the steel yielding core was calculated as:

$$A_{min} = \frac{45 \text{ kN}}{260 \text{ MPa}}$$

$$A_{min} = 173 \text{ mm}^2$$

The cross-sectional area was initially set as 15.875 mm [0.625"] x 12.7 mm [0.5"] which resulted in an area of 202 mm² and subsequently a predicted yield force of 52 kN.

The maximum allowable strain affects how long the device can be; however, a portion of the device still must be embedded in the foundation. Aiming to keep as much of the length of the device within the steel component as possible, the maximum allowable strain based on the effective length was selected as 15%, which is about 60% of the strain capacity of A36 steel, as shown in Figure 3.3.

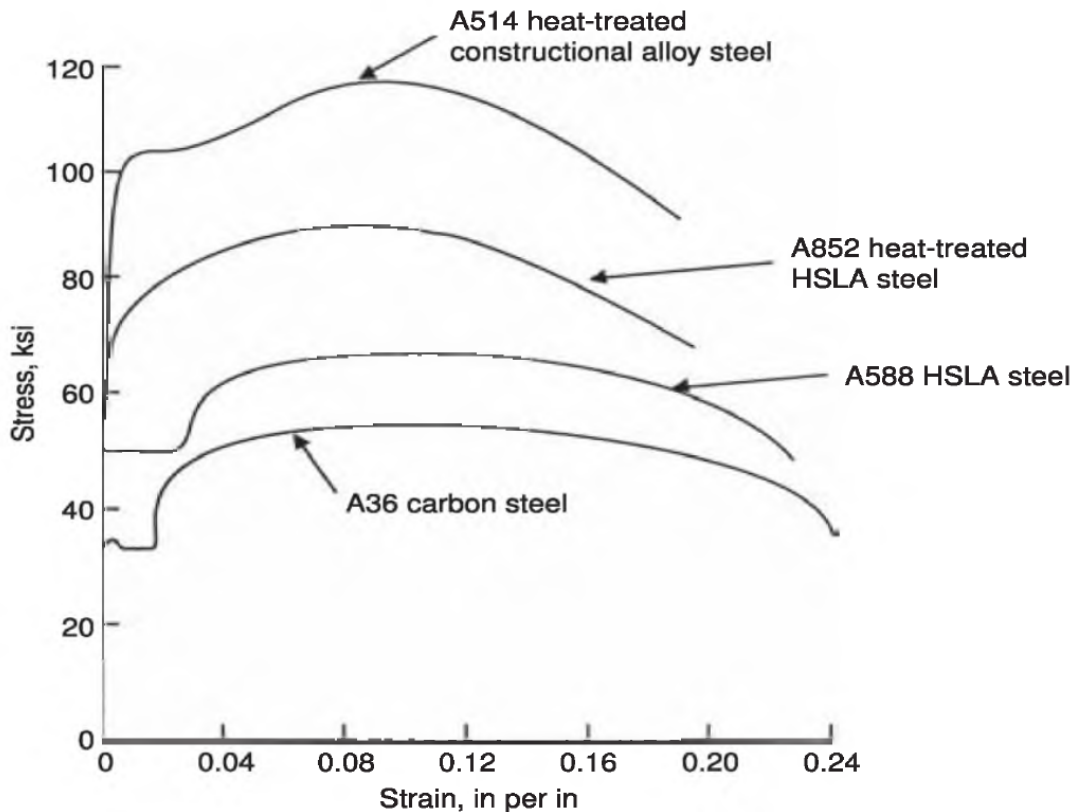


Figure 3.3: Stress-strain curves of common steel grades (Bruneau, 2011)

Knowing the uplift demand at the centre of the wall (23.5 mm) and selecting a maximum allowable strain (15%), the effective length for the device, $L_{effective}$, was calculated as:

$$\epsilon_{allowable} = \frac{\Delta_{uplift}}{L_{effective}} \quad (8)$$

$$(0.15) = \frac{(23.5 \text{ mm})}{L_{effective}}$$

$$L_{effective} = 157 \text{ mm}$$

3.2.3 Rubber Debonding Layer

As shown earlier in Figure 2.7, the minimum clearance of the debonding layer s_r is calculated as:

$$s_r \leq \frac{\nu_{steel} \epsilon_c t_c}{2} \quad (9)$$

Where ν_{steel} is 0.5, ϵ_c is the maximum strain allowed at 15%, and t_c is the core thickness of 12.7 mm [1/2"]. The minimum debonding layer thickness for the device is calculated as:

$$s_r \leq \frac{(0.5)(0.15)(12.7 \text{ mm})}{2}$$

$$s_r \leq 0.476 \text{ mm}$$

The chloroprene rubber was 0.793 mm [1/32"] as it was the smallest increment available for purchase.

3.2.4 Grout Design and Bracing Strength

In order to determine the required strength of the grout, the expected high mode wavelength should first be calculated. In turn, this requires EI_{eff} , described earlier in Section 2.2.3.2, was calculated as:

$$EI_{eff} = 0.055EI \quad (10)$$

$$EI_{eff} = 0.055 \left(\frac{(200 \text{ GPa})(15.875 \text{ mm})(12.7 \text{ mm})^3}{12} \right)$$

$$EI_{eff} = 29.8 * 10^6 \text{ Nmm}^2$$

Using the wavelength equation from Section 2.2.3.2 along with the calculated yield force in Section 3.2.2, the high mode wavelength of the device is:

$$L_w = \sqrt{\frac{4\pi^2(EI)_{eff}}{P_y}}$$

$$L_w = 150 \text{ mm}$$

As discussed in Section 3.1, the maximum assumed force to be experienced by the device is 45 kN. This value is taken as $P_{maximum}$, and assuming a device maximum allowable strain of 15%:

$$P_b = \frac{4(45 \text{ kN})[(2)(0.793 \text{ mm})+0.5(0.15)(12.7 \text{ mm})]}{150 \text{ mm}}$$

$$P_b = 3.049 \text{ kN}$$

Assuming that the lateral load P_b is applied to the grout as described in Equation 5, the required grout strength for the device calculated as 15 MPa. Cylinders that were tested during the casting stage of these devices showed an average grout strength of 57 MPa. Using Equation 4, the Demand Capacity Ratio of the design was calculated as 0.085, well under the 1.0 recommended limit discussed.

3.3 Test Instrumentation and Setup

The Shimadzu universal tester was used to apply uniaxial loads to the specimens. However, the machine did not have a cyclic test function. Therefore, an adapter for the Shimadzu was designed and built that allowed for unidirectional half cycles to be applied to the specimens. The specimen was tested in tension, both loading and unloading, and then was removed from the adapters and attached to the compression adapters to complete one cycle. Figure 3.4 shows the adapter attached to the Shimadzu tester, while Figure 3.5 shows the installation during calibration.

More details as well as full drawings of all three adapter pieces can be found in Appendix B. Since the end connections of the device were attached as a steel-on-steel connection as shown in Figure 3.1, the adapter was designed to simulate similar end fixities. The adapters were designed to minimize test setup slack while also facilitating the transitions between the tension and compression cycles of the testing.

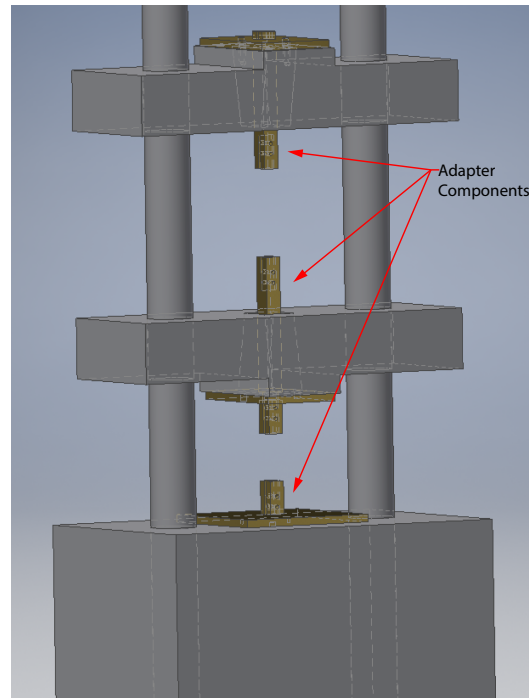


Figure 3.4: Schematic of adapter design



Figure 3.5: Full assembly of adapter installed into the Shimadzu

To account for the possibility of slack in the system, a string potentiometer was installed onto each device. The potentiometer was attached to the steel yielding core at the ends of the confining case to measure the core's displacement during the half-cycles, as shown in Figure 3.6.

The string potentiometer received the displacement readings of the effective length of the devices which then transmitted to the data acquisition machine. The housing for the string potentiometers was consistently placed 10 mm away from the cases as shown in Figure 3.7. Simultaneously, the force and displacement readings from the Shimadzu were sent to the data acquisition machine. A full schematic of all instrumentation is shown in Figure 3.8.



Figure 3.6: String potentiometer installation

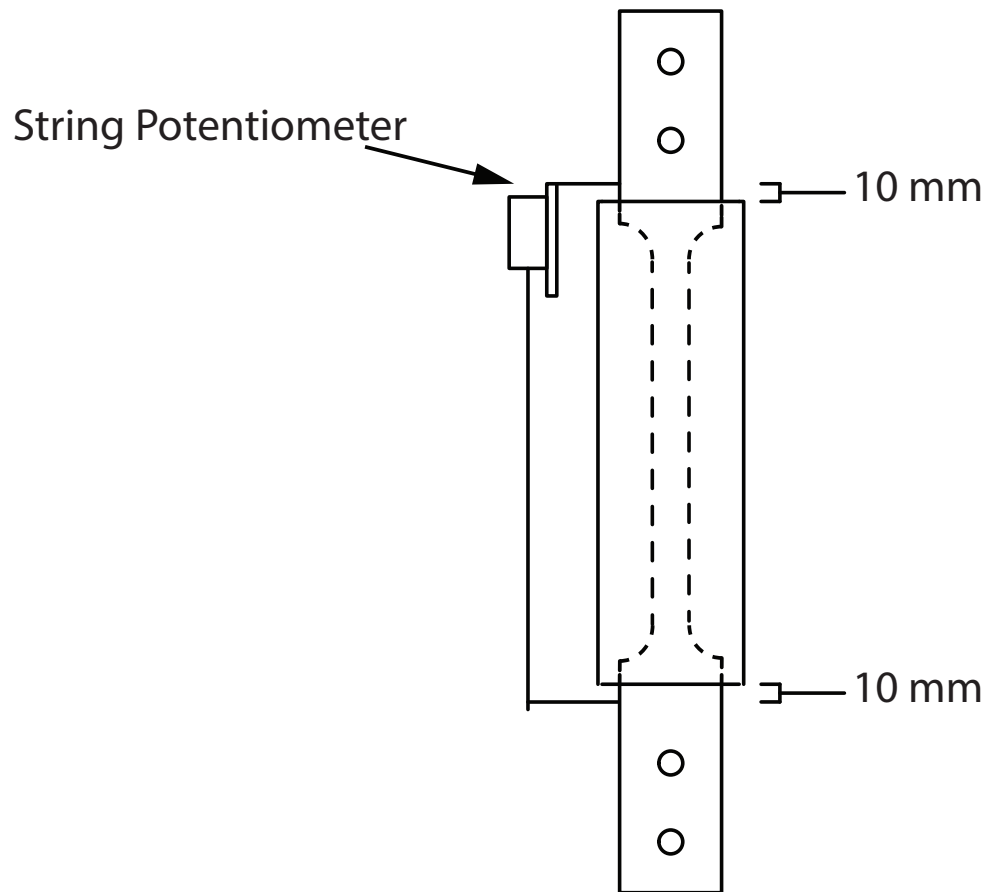


Figure 3.7: Installation of string potentiometers

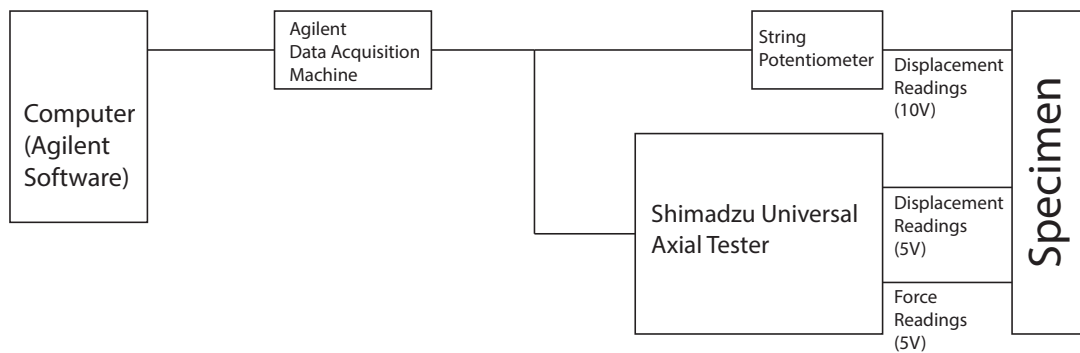


Figure 3.8: Full schematic of instrumentation

3.4 Construction Process

The construction process of these devices took multiple iterations to optimize. Construction began on multiple fronts: the rubber debonding layer, the steel, and grout. The rubber sheets are a neoprene compound with 0.793 mm [1/32"] thickness, based on Tsai et al. (2014). The grout for the device is made from Quikcrete, used for its ready-mix convenience.

The steel used for the yielding core was found to be challenging to machine in-lab, so it was sent out to be machined at the McMaster Manufacturing Research Institute (MMRI) to specifications shown in Figure 3.9. While the yielding core specimens were being machined, the steel cases were welded. Custom 0.125 mm [1/8"] steel cases were welded on-site at the ADL. This allowed the desired dimensions to be matched more accurately than what was possible with commercially available hollow structural sections (HSS). At full-scale, this may not be required. Figure 3.10 shows the cases assembled before the full length welds were completed.

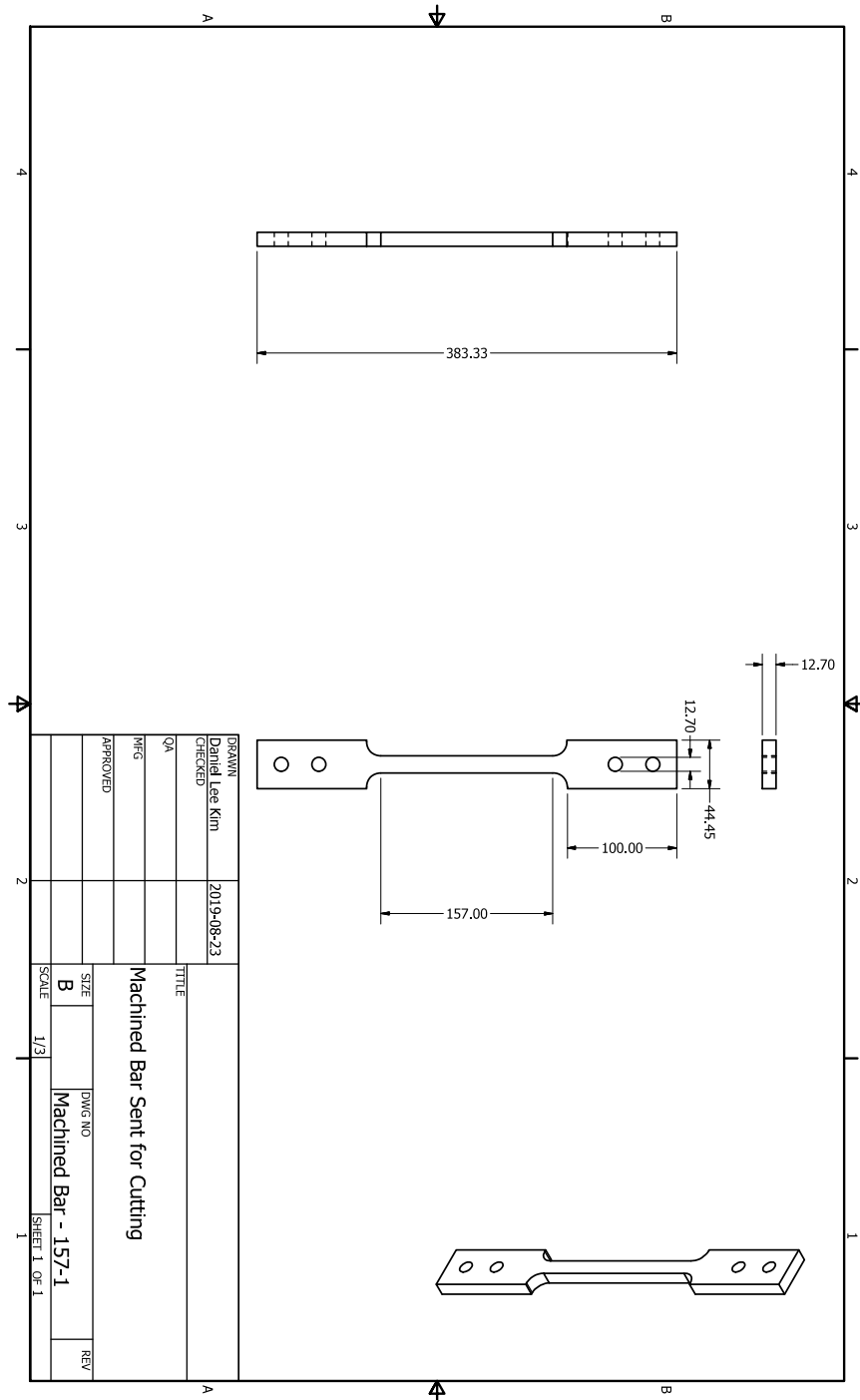


Figure 3.9: Custom cut steel yielding core



Figure 3.10: Confining case assembly before full weld

Neoprene rubber was then cut into pieces to cover the effective length of the yielding core exactly. REMA Tip Top SC2000 adhesive was used to ensure a durable application between the steel and neoprene rubber. However, before application, the steel yielding core surface was scored with a coarse sandpaper to increase adhesion, as shown in Figure 3.11. Once the adhesive was dry and the rubber bonded, the full specimen was lubricated with petroleum-based grease to act as a further lubricant between the rubber and grout. Finally, the specimens were casted by pouring the Quikcrete into the cases with the cores centered.



Figure 3.11: Preparation for rubber application

A batch of specimens were ordered and cut for tests. Steel slotted end plates were welded at one end of each specimen and using temporary wedges to ensure that each specimen was centered from both ends during casting, as shown in Figures 3.12, 3.13, and 3.14.



Figure 3.12: Temporary wedges used during grout pouring



Figure 3.13: Assembling specimens for casting

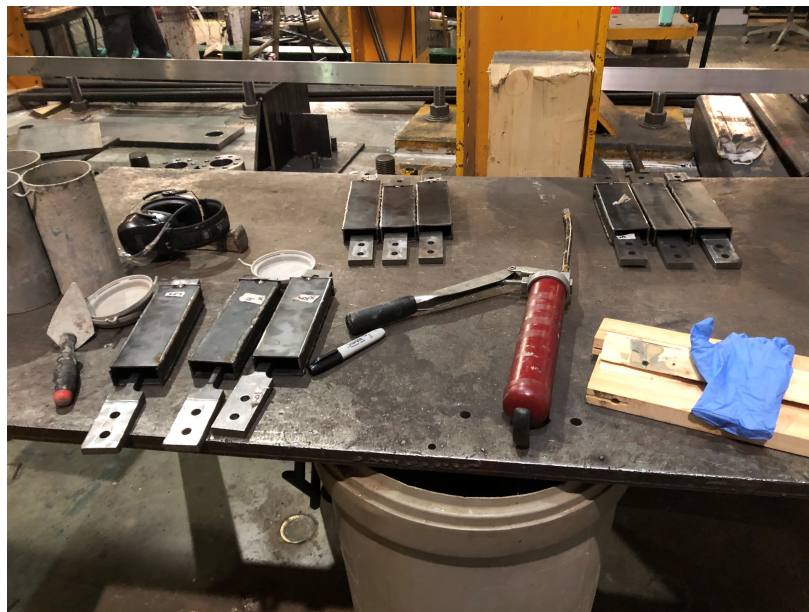


Figure 3.14: All specimens being prepared for casting

3.5 Parametric Study Schedule

Table 3.1 summarizes the tested specimens along with their corresponding yield strength, designed yield force, allowed maximum strain, effective length, debonding rubber thickness, and cross-section dimensions. Test duration for one specimen averaged about five hours, allowing for time to complete about one per day. The tests were conducted in their parametric study groups. The designed yield parameter was investigated to determine if the device can be scaled for different forces while the allowed strain and debonding rubber thickness parameters were investigated to determine their influence on the device's hysteretic behaviour.

The W series represents the number of times the effective length was wrapped in debonding rubber, while the VL series represents the modification of the effective length, and the XS series represents the designed yield force of the yielding core based on the cross-section area.

Table 3.1: Planned test schedule

		Specimen	Yield Strength (kN)	Analytical Yield (kN)	Allowed Strain	Effective Length (mm)	Unbonding Rubber (mm)	Cross Section (in x in)
1	RUBBER THICKNESS	0W	440	88.7	15%	157	0	0.625 x 0.5
		2W	440	88.7	15%	157	1.59	0.625 x 0.5
		3W	440	88.7	15%	157	2.38	0.625 x 0.5
2	EFFECTIVE LENGTH	VL SHORT	290	52.4	17%	138	0.8	0.625 x 0.5
		VL BASE	290	52.4	15%	157	0.8	0.625 x 0.5
		VL LONG	290	52.4	13%	181	0.8	0.625 x 0.5
3	CROSS SECTIONAL AREA	XS45	290	52.4	15%	157	0.8	0.625 x 0.5
		XS30	440	59.1	15%	157	0.8	0.4167 x 0.5
		XS23	440	44.3	15%	157	0.8	0.3125 x 0.5

3.6 Loading Protocol

The loading protocol for the specimens is a modified version of the unidirectional cyclic test as described in FEMA 461 (FEMA, 2007). As per FEMA 461, the loading protocol starts “at a displacement that can be repeated for six (6) cycles without visible damage to the specimen”. Each loading amplitude was repeated twice, then increased by 40%. This continued until the target displacement of 23.5 mm was reached. Once the target displacement was reached, the loading displacement was increased by 30% for each proceeding cycle until the device failed. The protocol generally requires that the loading amplitudes are applied in the positive (tension) and negative (compression) directions of the specimen. However, because of the designed installation of the device, the specimen was only tested within the positive domain. The tests were terminated when either the specimen fractured or the limitation of the test set up was reached. A sample loading protocol can be seen in Figure 3.15.

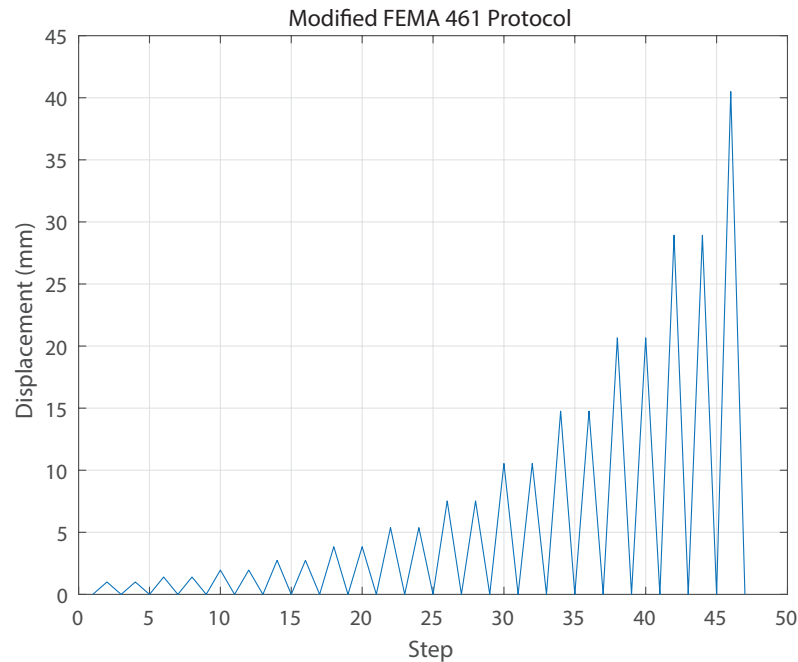


Figure 3.15: Planned loading protocol

3.7 Coupon Test Results

Figure 3.16 presents the results of each coupon test performed. The extensometer that was acquiring the data was removed prior to fracture in order to save the equipment from serious damage. Therefore, these figures do not fully present the ductility of each specimen. The first batch of steel had a slight overstrength compared to the specified yield strength of 260 MPa, resulting in a yield strength of 292 MPa. As can be seen in the figures, the average yield strength was 292 MPa and 440 MPa, for the first and second batches of steel, respectively. Although the second batch of specimens had higher strength, leading to higher than intended specimen strength, it also had a longer plastic plateau and a similar or higher strain capacity.

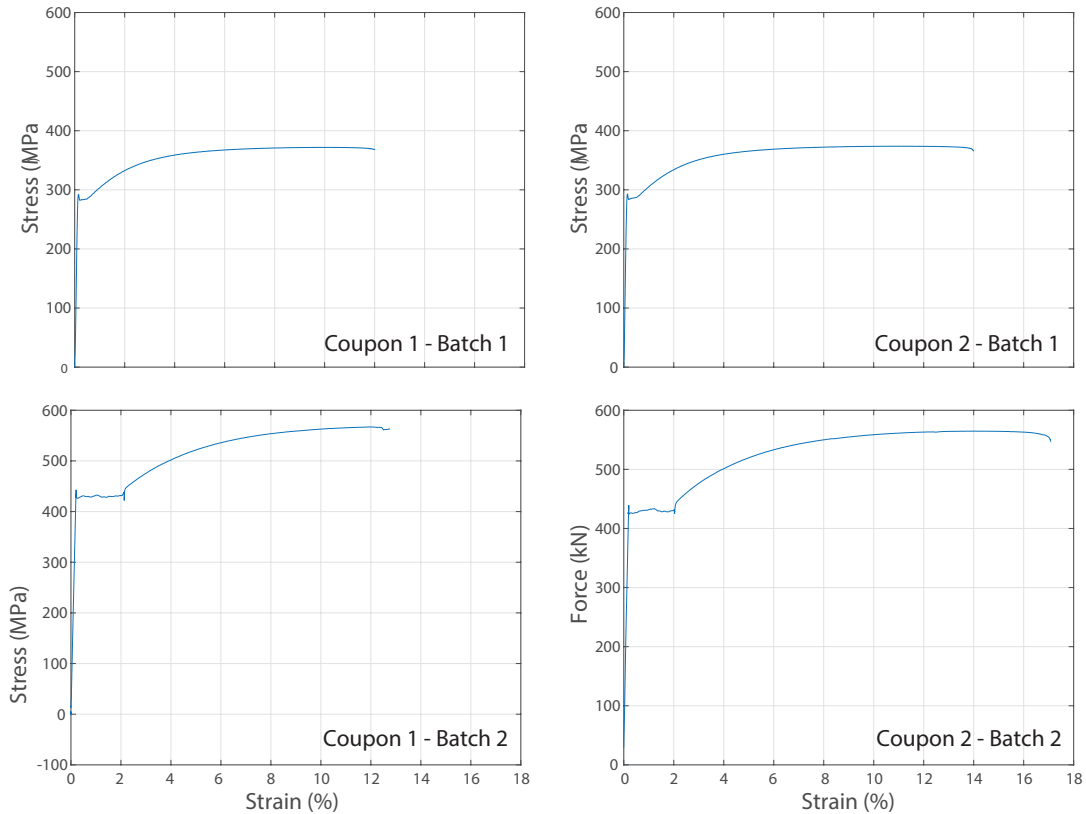


Figure 3.16: Coupons test results from both steel orders

3.8 Test Results

Figure 3.17 presents the experimentally observed hysteretic response of the devices tested in the current study. As can be seen in Figure 3.17, the displacement of the device is also presented as the corresponding wall drifts assuming that the device is installed in a CRMW at a distance of 950 mm from the centre of rotation. The base

specimen was tested twice: once as VL BASE, and once as XS45. Provided on each graph is the analytical yield force calculated using the actual strength of the steel used for each specimen. The following subsections discuss the findings of each parametric study performed.

The degradation in the specimens is caused when the yielding core has been extended from the restraining case and will be discussed further in Section 3.8.1. Hysteretic results show very slight strength degradation, suggesting that slight necking occurred which left the specimen more vulnerable to buckling at that location. Once displaced that far from the case, the yielding core was much more susceptible to degradation.

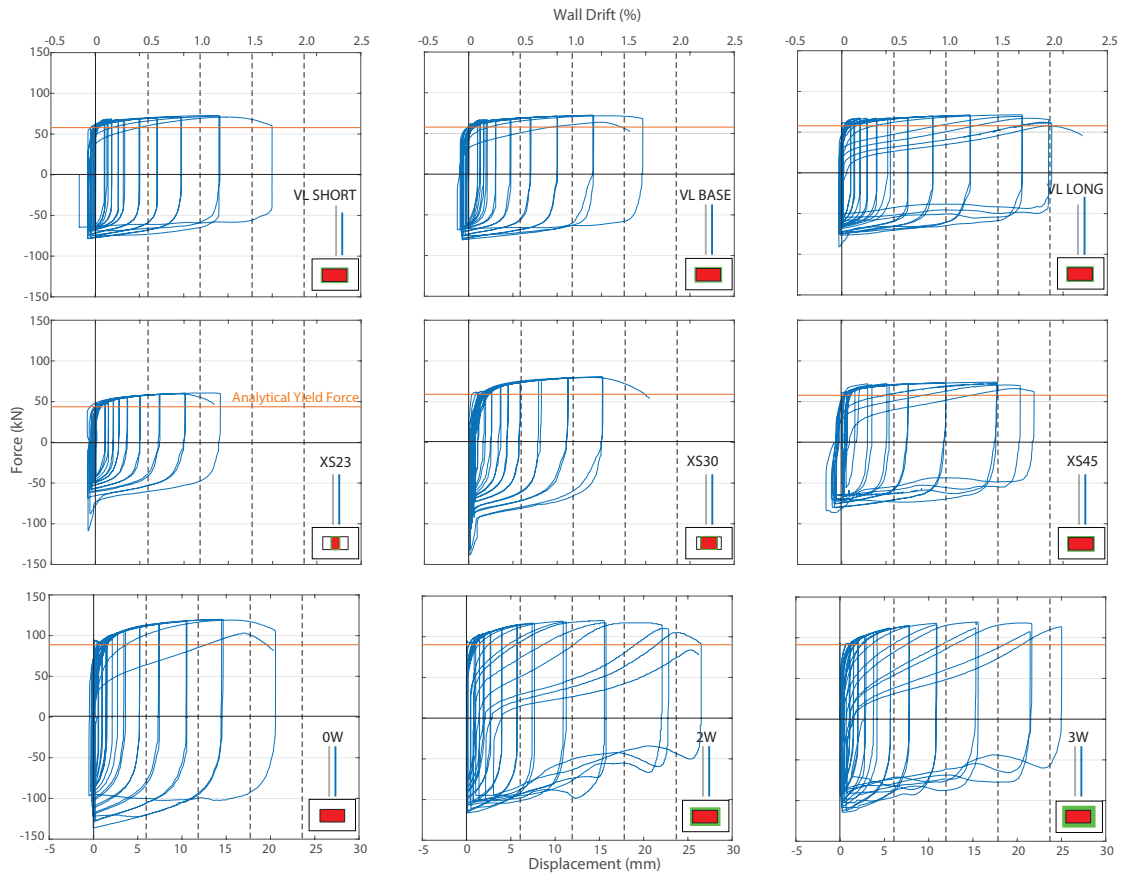


Figure 3.17: Experimental results

3.8.1 Effective Length Specimens

Figure 3.17 (top row) demonstrates that specimens VL SHORT, VL BASE, and VL LONG show nearly identical ultimate strength values of 55 kN, 57 kN, and 57 kN, respectively. This is expected since their cross-sectional areas were maintained regardless of the effective length changes provided in this study.

However, specimen VL LONG exceeded the target displacement of 23.5 mm with an ultimate displacement of 28 mm, whereas specimens VL SHORT and VL BASE

failed earlier at ultimate displacements of 20.5 mm and 20.7 mm, respectively. The longest specimen VL LONG was the only specimen to reach the target displacement because the allowable maximum strain was designed to be 13%. VL LONG began to exhibit stiffness degradation at about 20 mm [1.75% wall drift] once the yielding core began to buckle into the retaining case and damage it during the compression phase of the cycle. Figure 3.18 shows how far the yielding core is extended from the restraining case when degradation occurs. Observing test videos, the first visible buckling occurred during the first compression cycle at 14 mm [1.2% wall drift]. The permanent damage to the cases can be seen in Figure 3.19.



Figure 3.18: VL LONG Specimen: Yielding core after tension half-cycle



Figure 3.19: Permanent damage of retaining case

3.8.2 Cross-Sectional Area Specimens

Figure 3.17 (middle row) shows the experimental results of specimens XS30 and XS23 where the width of the yielding core was reduced by one-third and two-thirds, respectively. As seen in Table 3.1, XS45 was made from steel with a weaker yield strength, while XS30 and XS23 were from the stronger second order. This led to the similar yield force peaks for XS45 and XS30 of about 55 kN and 54 kN, respectively. A comparison between XS23 and XS30 shows that the hysteretic shapes are nearly identical, with the difference being in the yield forces that cause XS30 to have a larger value. If repeated with similar steel as XS23 and XS30, it is expected that XS45 should demonstrate higher strength performance – specifically an increase that is consistent with the difference between XS23 and XS30.

Specimen XS45 was the first specimen tested, which had its difficulties. The specimen was unintentionally tested differently from the loading protocol in Section 3.6 as the overall process was still being fully understood and optimized. This included errors such as incorrect testing duration during half-cycles that eventually led to the hysteretic behaviour differences between XS45 and VL BASE such as the “waves” in the compression cycles of XS45.

When evaluating XS23, the sudden increase in stiffness immediately after negative displacement was caused by the head of the specimen getting compressed into the grout. However, in XS30, the increase in stiffness only occurred due to some of the grout debris falling into the case during testing. This may be something to be considered in future work because if the grout debris falls into the case obstructing the movement of the yielding core, less energy can be dissipated until the debris is crushed.

Since the forces that specimens XS23 and XS30 experienced were less than the expected forces of the base design, at about 50 kN, the confining grout of these specimens were overdesigned. In comparison to other specimens, these two specimens showed the most consistent performance without degradation until their fracture. These findings suggest that stronger grout would ensure that detrimental damage would not occur in compression, while maintaining initial elastic stiffness throughout the loading protocol and preventing loss in strength during compression.

3.8.3 Rubber Thickness Specimens

Figure 3.17 (bottom row) shows results of specimens 0W, 2W, and 3W. The ultimate strength of these specimens was much higher at about 114 kN for all three specimens because they were made with the higher yield strength steel. Specimen 0W demonstrated the most reliable response of the three tests as the performance only started to decrease close to when necking occurred.

Specimens 2W and 3W showed strength and stiffness degradation much sooner when necking occurred, at about 14 mm [1.2%] and 7.5 mm [0.64%] respectively. Based on the results above, it is recommended that more than one layer of rubber can extend the lifespan of the device from a ductility standpoint but will also cause early buckling that leads to strength degradation.

Reaching a peak strength of more than 100 kN, the lateral forces applied on the grout from the buckling steel are much greater than originally anticipated. However, another factor that may be more impactful is due to the thicker rubber layer causing more friction rather than preventing it. When the rubber layer becomes too thick, it appears to no longer act as a layer that prevents friction between the grout and steel, ultimately causing stress concentrations in the grout leading to failure. Figure 3.20 shows both the grout being damaged as well the rubber getting pulled from the specimen during testing. This performance is very similar to the “waves” in

the performance of Toranzo-Dianderas' design as shown in Figure 2.11. Specimen 0W however, did not have this type of response since the steel and grout were only separated by the lubricant. If the grout was designed to withstand the forces that were being applied by the buckling core, it is expected that the compression response would be closer to that of XS23 and XS30.

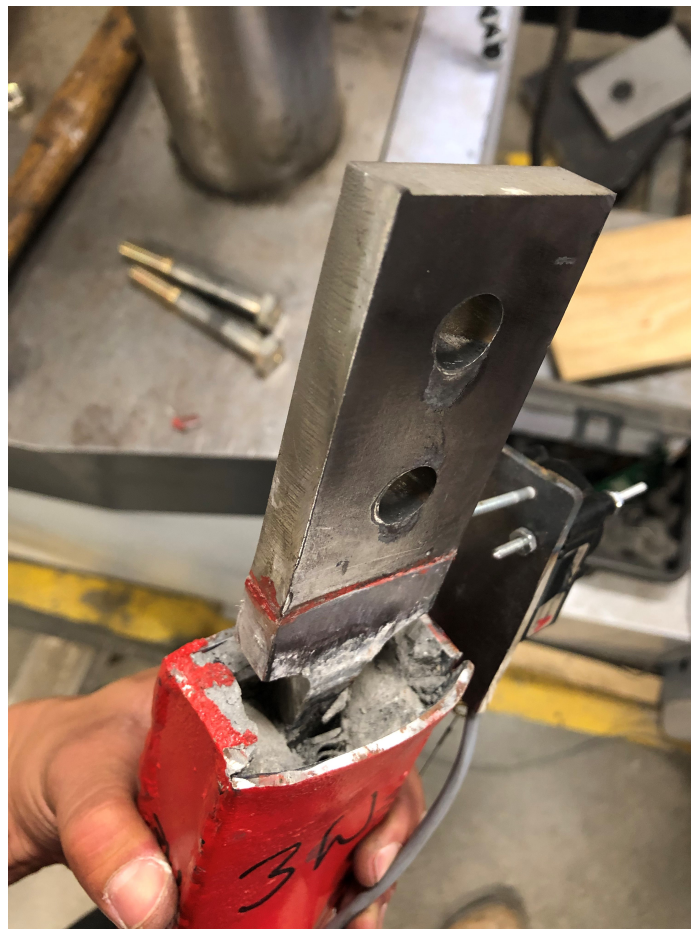


Figure 3.20: 3W Specimen: Rubber and grout damage

3.9 Ductility

Table 3.2 shows the ductility of each device with the ultimate displacement defined as the displacement at the specimen maximum strength. The ductility, μ , is calculated as the ratio between the largest repeatable displacement of the specimen (Δ_{ult}) and the displacement when a yield plateau was observed during testing (Δ_{yield}).

Figure 3.16 show that the coupon ductility was similar between both steel orders. Specimen VL LONG provided the greatest ductility at 22.81 mm/mm. This was expected since the target displacement of 23.5mm was designed to be reached at 13% strain. Specimens 2W and 3W show that additional rubber layers did improve ductility compared to the base specimens. Specimen 0W also showed that the lack of any rubber reduced the Δ_{ult} compared to the base specimens, further showing that the rubber slightly increase ductility.

Specimens XS23 and XS30 fractured very shortly after the maximum force was achieved while the specimens such as specimens 2W, 3W, and VL LONG were still able to be tested for multiple more cycles after achieving its maximum force. This suggests that the additional rubber layers did increase ductility while also confirming that the longer effective length extended the specimen's lifespan. While strength degradation did occur in those devices, none of them reached 80% strength during a cycle until fracture was imminent. It should be noted that specimen 3W was ended

in compression as the specimen began to reach the limitation of the test setup.

Table 3.2: Specimen ductility results

Specimen	Yield Strength (MPa)	Δ_{yield} (mm)	Δ_{ult} (mm)	Ductility (mm/mm)
XS45	292	1.20	17.62	14.68
VL BASE	292	1.02	15.00	14.75
0W	440	1.00	14.51	14.45
2W	440	1.03	22.08	21.43
3W	440	1.05	21.65	20.61
VL SHORT	292	1.46	13.93	9.53
VL LONG	292	1.03	23.50	22.81
XS30	440	1.06	15.16	14.35
XS23	440	1.07	10.16	9.49

3.10 Energy Dissipation

As a final metric to compare the devices, this subsection compares the energy dissipated through the area enclosed in each hysteretic cycle. To compute this, Matlab (MATLAB, 2017) was used to calculate the area under each half-cycle using the *polyarea* function. The total area of all half-cycles is added together to determine the total energy dissipation. After comparing the areas of each loop, Table 3.3 shows their total energy dissipated from least to greatest. The energy dissipated is a function of ductility and force capacity, therefore, specimens such as 2W dissipated a lot of energy although its hysteretic performance appears less desirable. Because the specimens used for the rubber thickness parametric study were fabricated from a stronger steel, the energy dissipation provided by those specimens was larger than that of

other specimens. Conversely, XS23 and XS30 as expected provided the least amount of energy dissipation. The change in energy dissipation is roughly proportionate to the change in cross-sectional area for the devices. Of note, VL SHORT showed an amount of energy dissipation similar to that of VL BASE, suggesting that between 15% and 17% allowable strain, results are not different. However, VL LONG at 13% strain shows 26% and 42% more energy dissipation than VL BASE and VL SHORT respectively. However, when normalizing the energy dissipation by the analytical field force of the steel core, the results show that the base design dissipates the most energy behind specimen VL LONG. The VL and XS series specimens show an expected trend in energy dissipated per kN while the W series specimens are rather inconclusive. This further suggests that the parametric study for that test may need to be repeated.

Table 3.3: Specimen energy dissipation results

Specimen	Energy Dissipation (kJ)	Energy Dissipation / F_y (kJ/kN)
XS45	16.69	0.319
VL BASE	15.77	0.301
0W	23.71	0.267
2W	25.01	0.282
3W	23.33	0.263
VL SHORT	14.00	0.267
VL LONG	19.93	0.380
XS30	13.69	0.232
XS23	9.03	0.204

Figure 3.21 shows the energy dissipated during each cycle, while Figure 3.22 shows the cumulative energy dissipation of each device at each cycle. VL SHORT and VL BASE dissipated almost similar amounts of energy throughout the loading his-

tory. However, VL LONG dissipated less energy per cycle compared to these specimens as less of the deformation in VL LONG comes from yielding of the entire core and more from the elastic deformations.

Since specimen XS45 was subjected to initial testing difficulties mentioned earlier, the energy was not actually dissipated in the first few cycles. However, at later stages of loading, the expected variation in energy dissipation due to cross-sectional area is successfully shown.

The rubber thickness influenced the energy dissipation per cycle. The key feature of note is the size of the jagged increase for specimens 2W and 3W. The repeated cycle of each amplitude in the loading protocol reduced the amount of energy that was dissipated. Reviewing test video, this was caused by empty space within the steel case that was created during the compressive cycles. When the restraining grout was damaged and the case was permanently deformed, a large void was created. On the second compression cycle at that amplitude, the empty space where the grout originally was becomes filled by the buckling steel core. The result is minimal increase or decrease in force while the displacement continues to decrease in compression. With additional rubber thickness, this empty space is even larger, showing that applying rubber debonding layers do not necessarily enhance overall performance if the debonding layer is too thick. Specimen 0W, with no rubber at all, did not experience any of

these dips in energy per cycle. However, if the grout was designed to withstand the test forces, it is unlikely that this would occur.

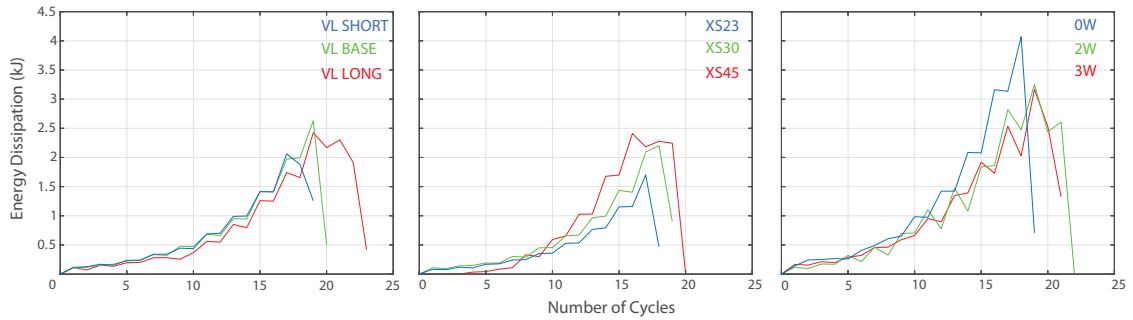


Figure 3.21: Comparison of specimen energy dissipation

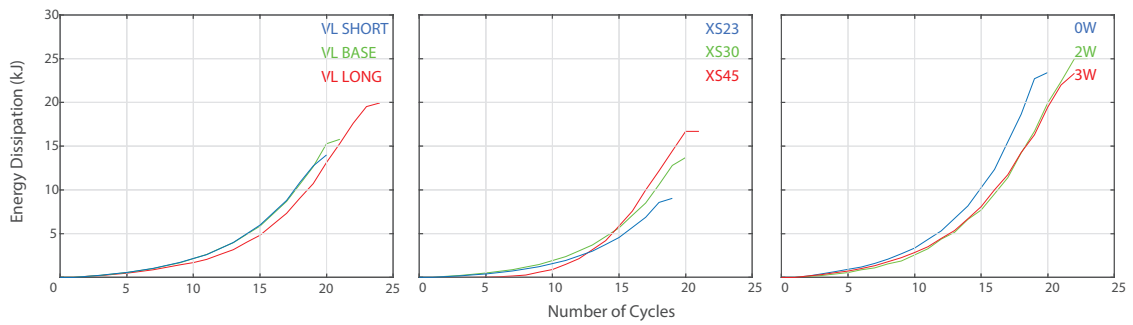


Figure 3.22: Comparison of cumulative specimen energy dissipation

4 NUMERICAL MODELLING

4.1 Modelling Approach

The current section presents a numerical OpenSees model that can capture the hysteretic performance of the tested devices without performing computationally intensive analysis. This model can be used in future studies in a global model of a CRMW that contains this device.

Observing the test results, the majority of the response of all specimens is primarily bilinear. The Steel4 and MinMax materials available in OpenSees were used to capture the response of the experimental specimens. Steel4 was used for its multiple parameters that facilitate properly shaping the hysteresis. As mentioned earlier in Section 2.3.2, Steel4 builds upon the Steel02 material, but has additional key features, namely the ability to create an asymmetric hysteretic response and specify ultimate tension and compression forces. However, Steel4 does not have a fracture strain, therefore the MinMax material is wrapped over the Steel4 properties to allow for failure of the specimen.

4.2 OpenSees Model

4.2.1 Model Overview

The OpenSees model is designed as shown in Figure 4.1.



Figure 4.1: Schematic diagram of the OpenSees model

The performance of the new device has an initial stiffness that includes more than just the stiffness of the yielding core. Rather, the entire cross section – the yielding core, grout, and steel case – acts as one. This can be seen from the comparison shown in Figure 4.2, where both models are identical, only changing the value of the effective elastic modulus, E , between 200 GPa and the calculated 947 GPa, as will be discussed in detail next.

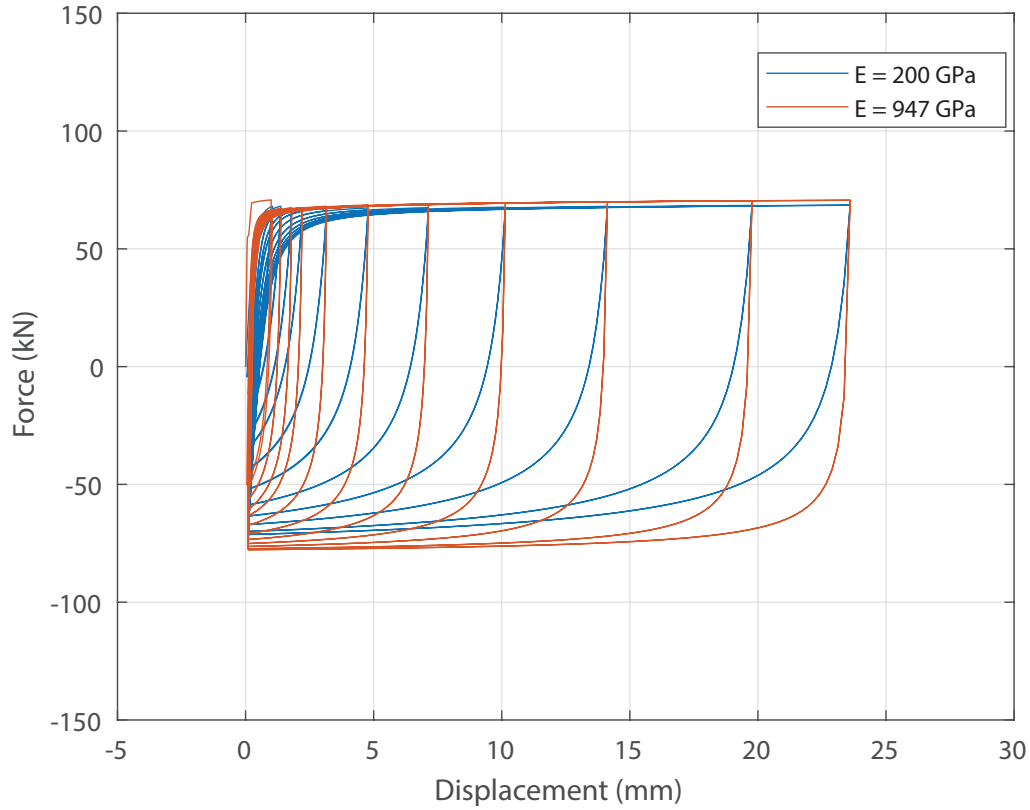


Figure 4.2: Comparison of steel elastic modulus and device elastic modulus

The initial stiffness of the model is calculated as:

$$E_{steel}(A_{case} + A_{core}) + E_{grout}A_{grout} = E_{effective}A_{effective} \quad (11)$$

E_{steel} is 200 GPa and λ_{grout} 1600kg/m³ (RBC Surveyors, 2019). Following CSA A23.3 (CSA, 2014a) standards, E_{grout} is:

$$E_{grout} = (3300\sqrt{f'c} + 6900)\left(\frac{\lambda_c}{2300}\right)^{1.5} \quad (12)$$

$$E_{grout} = 18.45 \text{ GPa} \quad (13)$$

The OpenSees model is designed as the effective length of the specimen, and therefore has an effective uniform cross-sectional area that is equal to that of the yielding core.

The effective modulus of elasticity is calculated as:

$$E_{effective} = \frac{E_{steel}(A_{case} + A_{core}) + E_{grout}A_{grout}}{A_{effective}} \quad (14)$$

$$E_{effective} = 947 \text{ GPa} \quad (15)$$

Steel4's asymmetrical abilities were used to capture the different post-yield stiffness of the device in tension and compression in order to get a better representation of the device in both cycles.

4.2.2 Model Validation

Figure 4.3 shows a comparison between the experimental and model results for specimen VL BASE:

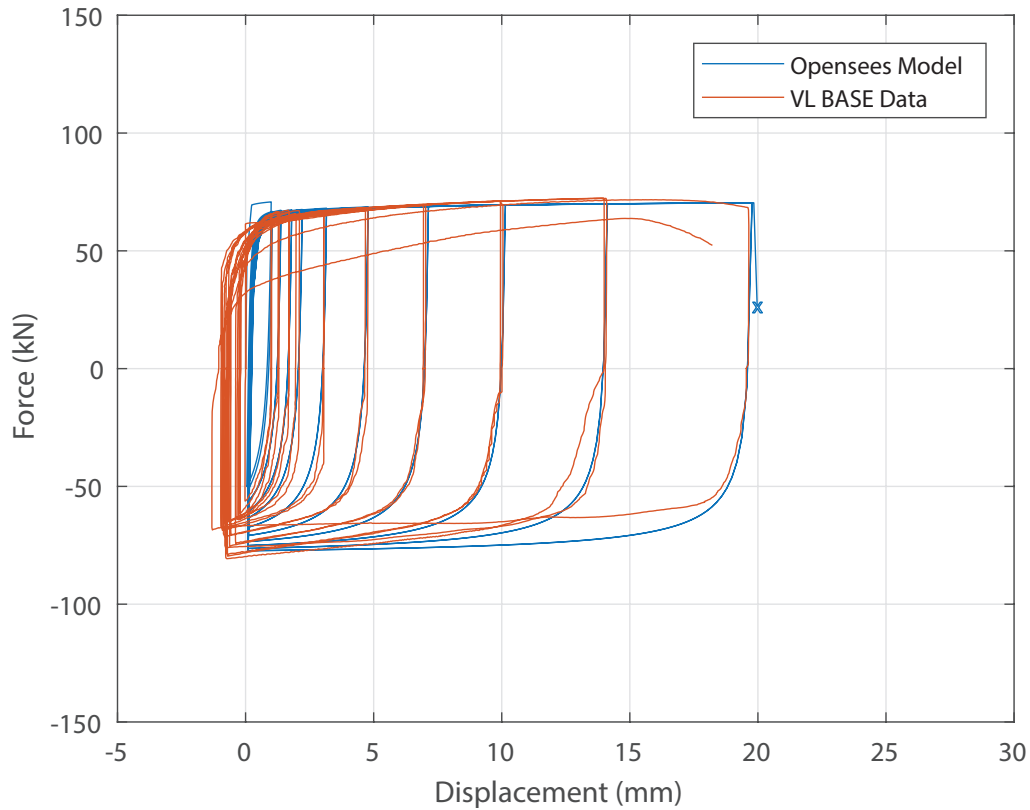


Figure 4.3: Steel4 MinMax model compared to VL BASE experimental results

As can be seen in the figure, the model and experimental results are in good agreement with only minor discrepancies at late loading stages in tension and compression. In the first tension cycle of the OpenSees Model, the specimen achieves a higher yield force then begins plateauing. It never reaches this force for the remaining duration of the test. However, Steel4 allows for a specified secondary stiffness as a ratio of post-yield stiffness to elastic stiffness. It is expected that if the model was allowed to displace long enough that the secondary stiffness would eventually reach and plateau at the same peak value. The MinMax material is able to define the point of fracture,

as once it is reached, the forces in the system become zero.

The OpenSees model was further modified for specimens 0W and XS23 to evaluate the sensitivity of the model to changes in steel strength and cross-sectional area, respectively. In order to account for the increase in compressive strength, the ultimate force in compression was calculated for 0W from the experimental results.

All other parameters of the Steel4 material were unchanged, while the MinMax material was modified to represent the change in fracture point. The fracture point was specified as the displacement at which the experimental specimens failed. Tables 4.1 and 4.2 show the parameters used in Steel4 and MinMax respectively. The parameters that were changed are in bold text. Note that while yield and ultimate forces in tension are provided in kN, the model took the value of the coupon stresses multiplied by the cross-sectional area.

Table 4.1: Steel4 Parameters

Specimen:		VL BASE and XS23	0W
Steel4 Parameters	F_y	58.7 kN	88.4 kN
	E_0	947 GPa	947 GPa
	b_i	0.2	0.2
	ρ_i	0.5	0.5
	b_l	0.15	0.15
	R_i	0.1	0.1
	l_{yp}	1.0	1.0
	b_{ic}	0.2	0.2
	ρ_{ic}	0.9	0.9
	b_{lc}	0.2	0.2
	R_{ic}	0.4	0.4
	b_k	0.1	0.1
	R_0	20	20
	r_1	0.9	0.9
	r_2	0.15	0.15
	b_{kc}	0.85	0.85
	R_{0c}	20	20
	r_{1c}	0.9	0.9
	r_{2c}	0.15	0.15
	f_u	74.6 kN	116.58 kN
R_u	0.4	0.4	
f_{uc}	80.4 kN	140.7 kN	
R_{uc}	0.8	0.8	

Table 4.2: MinMax Parameters

Specimen:		XS23	0W	VL BASE
MinMax Parameters	<i>Min</i>	$1 * 10^{-16}$ (Default)	$1 * 10^{-16}$ (Default)	$1 * 10^{-16}$ (Default)
	<i>Max</i>	14.7	20.6	20.0

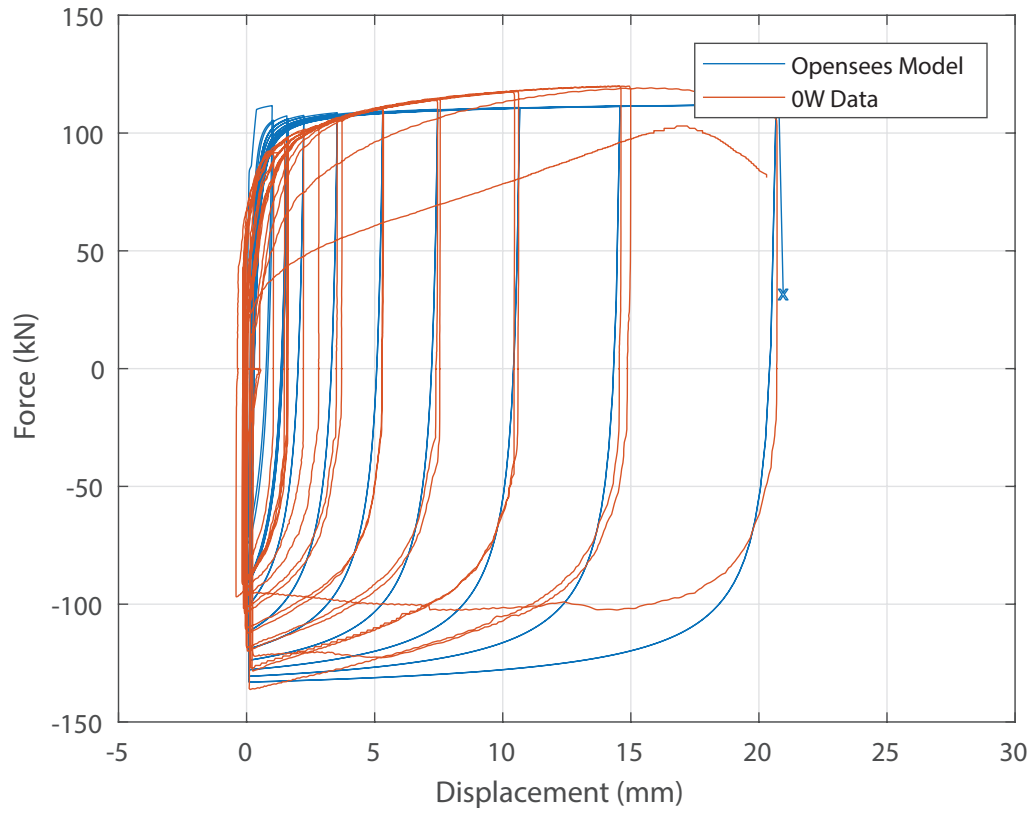


Figure 4.4: Steel4 MinMax model compared to 0W experimental results

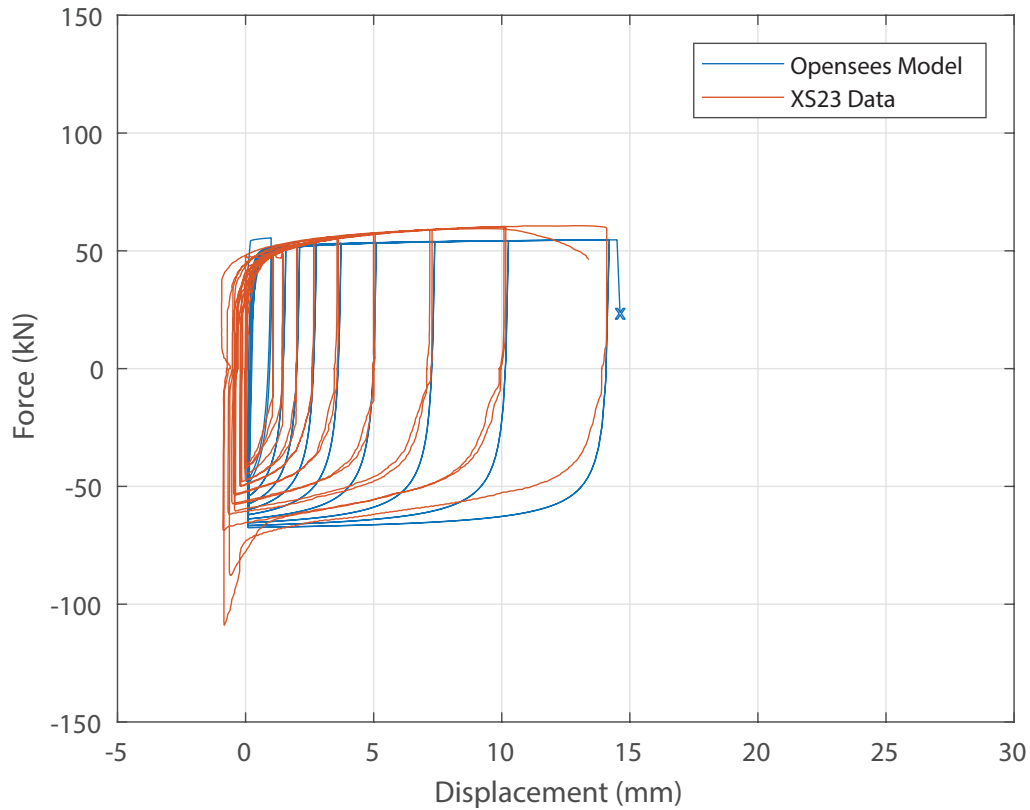


Figure 4.5: Steel4 MinMax model compared to XS23 experimental results

Figures 4.4 and 4.5 show the OpenSees model provides acceptable results compared to the experimental counterparts with minimal errors for specimens XS23 and 0W. The VL series specimens were not modelled as the effective length does not affect the model. Further, 2W and 3W were not modelled as the model is not capable of capturing the degradation shown in the experimental results of those specimens. Table 4.3 shows the force values where the OpenSees model and the experimental results appear to vary. The largest discrepancy is particularly in compression, where the model overestimates strength by about 20%. The largest error discrepancies are close

to 20%, but only for small portions of the response. Overall shape of the hysteretic responses is still quite similar for the majority of the loading protocol.

Table 4.3: Comparison between OpenSees model and experimental results

Specimen		Experimental Force (kN)	OpenSees Force (kN)	Error (%)
VL BASE	Tension	72	70	-2.77
	Compression	45	55	+18.18
0W	Tension	117	111	-5.13
	Compression	102	113	+9.73
XS23	Tension	60	54	-10.00
	Compression	52	62	+19.23
XS30	Tension	80	73	+8.75
	Compression	70	78	-11.43

5 SUMMARY AND CONCLUSIONS

5.1 Summary

This thesis proposed an axial yielding energy dissipation device that can be installed in CRMWs. The device takes inspiration from buckling restrained braces; however, a much smaller scale compared to that of its initial installation into high-rise structures in the 1990's. The device is expected to be bolted into a steel section at the wall base to allow for simple replaceability following a seismic event. By using a combination of controlled rocking and the new energy dissipation device, masonry walls are expected to have only minimal damage, thus minimizing the shutdown time for structural repairs and replacement before the structure can be reoccupied.

Nine specimens were designed and created to investigate how the performance would change when modifying the cross-sectional area, effective length, and thickness of the rubber debonding layer. The specimens were tested on a Shimadzu universal axial tester in the Applied Dynamics Lab at McMaster University. Adapters were designed and installed to the universal tester to perform the testing. Once the experimental testing was concluded, an OpenSees model was developed to simulate the response of the tested specimens.

5.2 Conclusions

Overall, the base design of the specimens had a relatively stable hysteretic performance although most specimens did not reach the desired ultimate displacement. In order to ensure that these objectives are met, it is recommended that the design is limited to 13% maximum allowable strain while also increasing the grout strength to ensure its ability to sustain the lateral forces during compression to prevent the decrease in initial elastic stiffness in the following tension phases.

Specimen VL LONG fully completed the loading protocol up to a wall drift of 2.0% and subsequently showed a high displacement capacity compared to that of other specimens with smaller lengths. This indicates that the device length should be carefully designed and selected, thus limiting maximum strain to no more than 13% rather than the 15% currently used in the design.

Specimens XS23 and XS30 showed that the hysteretic performance of the device can be scaled depending on the yield force of the steel core. The performance of XS23 shows that at designed forces, about 50 kN maximum, the oversized grout was able to properly brace the yielding core and prevent any significant degradation. Overall, the tests showed that the grout should be designed stronger compared to the yield force of the steel core than what was selected for the base design. Stronger grout would ensure that detrimental damage does not occur in compression, maintaining

initial elastic stiffness throughout the loading protocol while also preventing loss in strength during compression.

The rubber thickness study showed that applying no rubber to the device can actually provide repeatable performance until fracture. However, the inclusion of one rubber debonding layer has increased the ductility of the device but specimens 2W and 3W had mixed results. However, the compression response of these specimens is expected to be much more stable as the grout is designed to withstand the lateral buckling forces. For further testing, the rubber thickness parametric study should be performed in tandem with other tests of the same steel strength and properly designed strength to fully understand the differences in performance.

A model was developed using OpenSees to simulate the performance of the new axial yielding device. The model used the Steel4 material which was capable of capturing asymmetric behaviour, the effects of nonlinear isotropic and kinematic hardening, and also gave the ability to define ultimate stress or force in the material. The Min-Max material was wrapped around the Steel4 to include fracture to the model. The initial elastic stiffness of the device was modelled as the effective stiffness of the full cross-section of the device rather than the steel yielding core on its own.

Using the experimental results, the OpenSees model was validated against the

performance of specimens VL BASE, XS23, and 0W. The model was able to capture the cyclic response of all three specimens. The model overestimated the experimental results only in small areas, mainly in compression. This appears to be inherent of Steel4 since the primary modifier for the elastic and post-yield stiffnesses are through ratios between those values. Better agreement could be achieved, but it would require individually remodelling each model rather than having a set group of values while the steel strength and cross-sectional area are modified. However, the model remained conservative for the majority of the simulation. While the fracture of the model can be specified, it was unable to predict when the fracture occurred through low-cycle fatigue.

5.3 Recommendations for Future Research

Experimental research for this device has been limited in the current study to quasi-static cyclic loading at half-scale testing with a limited range of geometrical configurations due to constraints associated with the testing apparatus. Further additional tests would be very useful to further understand the effects of modifying the restraining grout in an effort to establish an upper bound of effectiveness for that component specifically.

The OpenSees model performed well for the majority of the loading protocol; however, it briefly deviated from the experimental results particularly in compres-

sion. This should be addressed in future studies to improve the compressive response. In addition, while the model performed well in capturing the shape of the hysteresis, it was not able to provide a predicted fracture point. A low-cycle fatigue model integrated to approximate fracture would further improve the developed model.

Future steps include full implementation of the developed device into the specially designed CRMWs to investigate the system's overall performance during quasi-static cyclic loading and eventually dynamic loading. This includes both the physical connections to the wall and foundation, as well as the overall system-level behaviour of a CRMW that includes this device. Once all described studies have been completed, life-cycle and cost-benefit analyses of the proposed device should be performed.

6 REFERENCES

Berlinger J., Castillo M., Sanchez R. 2017. Mexico's strongest earthquake in a century leaves dozens dead. CNN, 9 September 2017. [Online]. Available: <http://www.cnn.com/2017/09/08/americas/earthquake-hits-off-the-coast-of-southern-mexico/index.html>. [Accessed 2017 November 28].

Bruneau, M. 2011. Ductile Design of Steel Structures. United States of America: The McGraw-Hill Companies, Inc.

CISC (Canadian Institute of Steel Construction). 2014. Commentary on CSA Standard S16-14 Design of steel structures. Mississauga, ON.

CSA (Canadian Standards Association). 2014a. CSA Standard A23.3-14 Design of concrete structures. Mississauga, ON.

CSA (Canadian Standards Association). 2014b. CSA Standard S16-14 Design of steel structures. Mississauga, ON.

Clark, P. W., Kasai, K., Aiken, I. D., Kimura, I. 2000. Evaluation of design methodologies for structures incorporating steel unbonded braces for energy dissipation. *Proceedings of the 12th World Conference on Earthquake Engineering*, Auckland, NZ.

Cook, J., Rodgers, G. W., Macrae, G. A., Chase, J. G. 2015. Experimentation with tension-only devices for use with seismic energy dissipation systems. *Proceedings of the 10th Pacific Conference on Earthquake Engineering*, Sydney, AU.

FEMA (Federal Emergency Management Agency). 2007. Interim Testing Protocols for Determining the Seismic Performance Characteristics of Structural and Nonstructural Components. Report FEMA 461. Washington, DC.

Filippou, F. C., Popov, E. P., Bertero, V. V. 1983. Effects of Bond Deterioration on Hysteretic Behaviour of Reinforced Concrete Joints. Berkley, CA: National Science Foundation.

Fujimoto, M., Wada, A., Saeki, E., Takeuchi, T., Watanabe, A. 1990. Development of Unbonded Brace 1990. *Quarterly Column*, 115, 91-96.

Hassanli, R., Elgawady, M. A., Mills, J. E. 2017a. In-plane flexural strength of unbonded post-tensioned concrete masonry walls. *Engineering Structures*, 136, 245-260.

Hassanli, R., Elgawady, M. A., Mills, J. E. 2017b. Simplified approach to predict the flexural strength of self-centering masonry walls. *Engineering Structures*, 142, 255–271.

Iwata Y., Sugimoto H., Kuwamura H. 2005. Reparability limit of steel structural buildings based on the actual data of the Hyogoken-Nanbu earthquake. *Proceedings of the 38th Joint Meeting of the U.S.-Japan Panel on Wind and Seismic Effects*, Gaithersburg, MD.

Kovacs, M., Wiebe, L. 2016. Seismic Design of Heavy Timber in Low-to-Moderate Seismic Hazard Regions. Master's Thesis. McMaster University. Hamilton, ON.

Laursen, P. T., Ingham, J. M. 2001, Structural Testing of Single-Storey Post-Tensioned Concrete Masonry Walls. *Journal of the Masonry Society*, 19(1), 69-82.

Laursen, P. T., Ingham, J. M. 2004, Structural Testing of Enhanced Post-Tensioned Concrete Masonry Walls. *ACI Structural Journal*, 101(6), 852-862.

Laursen, P. T. 2008. Seismic Performance of Prestressed Concrete Masonry Walls Incorporating Energy Dissipators. *Proceedings of the 14th World Conference on Earthquake Engineering*, Beijing, CN.

Lin, P.-C., Tsai, K. C., Chang, C.-A., Hsiao, Y.-Y., Wu, A. C. 2016. Seismic design and testing of buckling-restrained braces with a thin profile. *Earthquake Engineering & Structural Dynamics*, 45, 339–358.

MATLAB. 2017. version 9.3.0 (R2017b). Natick, MA: The MathWorks Inc.

Marriott, D., Pampanin, S., Palermo, A. 2009. Quasi-static and pseudo-dynamic testing of unbonded post-tensioned rocking bridge piers with external replaceable dissipaters. *Earthquake Engineering and Structural Dynamics*, 38, 331–354.

McCormick, J., Aburano, H., Ikenaga, M., Nakashima, M. 2008. Permissible Residual Deformation Levels for Building Structures Considering both Safety and Human Elements. *Proceedings of the 14th World Conference on Earthquake Engineering*, Beijing, CN.

Menegotto, M., Pinto, P. E. 1973. Method of Analysis for Cyclically Loaded R. C. Plane Frames Including Changes in Geometry and Non-Elastic Behavior of Elements under Combined Normal Force and Bending. *Proceedings of IABSE Symposium*, 15–22.

OpenSees. 2016. Open system for earthquake engineering simulation (OpenSees), v2.5.0. Berkeley, CA: Pacific Earthquake Engineering Research Center.

Priestley M. J. N., Elder D. M. 1983. Stress-Strain Curves for Unconfined and Confined Concrete Masonry. *ACI Structural Journal*, 80, 192-201.

Rahnavard, R., Naghavi, M., Aboudi, M., Suleiman, M. 2018. Investigating modeling approaches of buckling-restrained braces under cyclic loads. *Case Studies in Construction Materials*, 476–488.

RBC Surveyors 2019. "Conversion Tables for Aggregates," RBC Surveyors. [Online]. Available: <https://www.rbcsurveyors.co.uk/building-consultant/conversion-tables/>. [Accessed 2019 August 22].

Rosenboom, O. A., Kowalsky, M. J. 2004. Reversed In-Plane Cyclic Behavior of Posttensioned Clay Brick Masonry Walls. *Journal of Structural Engineering*, 130(5), 787–798.

Sabelli, R., Mahin, S., Chang, C. 2003. Seismic demands on steel braced frame buildings with buckling-restrained braces. *Engineering Structures*, 25(5), 655–666.

Sarti, F., Palermo, A., Pampanin, S. 2016. Fuse-Type External Replaceable Dissipaters: Experimental Program and Numerical Modeling. *Journal of Structural Engineering*, 142(12), 04016134.

Shi, Q., Wang, F., Wang, P., Chen, K. 2018. Experimental and numerical study of the seismic performance of an all-steel assembled Q195 low-yield buckling-restrained brace. *Engineering Structures*, 176, 481–499.

Steele, T. C., Wiebe, L. D. A. 2016. Dynamic and equivalent static procedures for capacity design of controlled rocking steel braced frames. *Earthquake Engineering & Structural Mechanics*, 45, 2349-2369.

Takeda, T., Takemoto Y., Furuya Y. 1972. An experimental study on moment frame with steel braces Part 3, *Summaries of Technical Papers of Annual Meeting Architectural Institute of Japan*, 47, 1389-1390.

Takeuchi, T. 2018. Buckling-Restrained Brace: History, Design and Applications. *Proceedings of the 9th International Conference on Behaviour of Steel Structures in Seismic Areas*, Christchurch, NZ.

Takeuchi, T. & Wada, A. 2017. Buckling-Restrained Braces and Applications. Japan

Society of Seismic Isolation.

Toranzo-Dianderas, L. A. 2002. The Use of Rocking Walls in Confined Masonry Structures: a Performance-Based Approach. Ph.D. Thesis. University of Canterbury. Christchurch, NZ.

Tsai, K. C., Wu, A. C., Wei, C.-Y., Lin, P.-C., Chuang, M.-C., Yu, Y.-J. 2014. Welded end-slot connection and debonding layers for buckling-restrained braces. *Earthquake Engineering & Structural Dynamics*, 43, 1785–1807.

Usami, T., Wang, C., & Funayama, J. 2012. Developing high-performance aluminum alloy buckling-restrained braces based on series of low-cycle fatigue tests. *Earthquake Engineering & Structural Dynamics*, 41, 643–661.

Wiebe, L. D. A. 2013. Design of Controlled Rocking Steel Frames to Limit Higher Mode Effects. PhD Thesis. University of Toronto. Toronto, ON.

Yassin, Ahmed (2018). Personal interview. December 2017.

Zsarnóczyay, Á. (2013). Experimental and Numerical Investigation of Buckling Restrainted Braced Frames for Eurocode Conform Design Procedure Development. PhD Thesis. Budapest University of Technology and Economics. Budapest, HU.

A BASE DESIGN CONNECTIONS

Included in the Appendix of this thesis are the calculations for the connection ends of the base design of the specimen and the design of the Shimadzu adapter. All equations in this section are referenced from CISC Handbook (CISC, 2014).

Since the tapered effective length of the steel yielding core is designed to yield before the rest of the device, the drilled hole connections at the ends of the device must be checked to ensure that yielding or failure does not occur.

The base specimen is designed to hold a maximum force of 45 kN per device. According to Table 3-4, the factored shear resistance for an ASTM A490 (now categorized under ASTM F3125) 1/2" bolt with threads excluded is 63.1 kN. Two bolts are selected for stability as seen in Figure A.1. In addition to accounting for double shear, this yields a total factored bolt shear resistance of 252 kN. Unfactored resistance is about 315 kN.

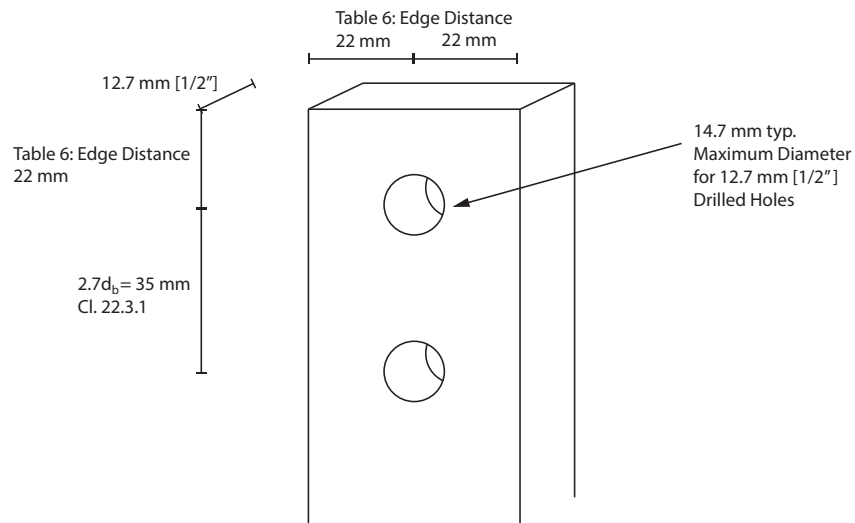


Figure A.1: Base connection design

The unfactored block shear resistance (Clause 13.11) can be found as:

$$T_r = [U_t A_n F_u + 0.6 A_{gv} \frac{(F_y + F_u)}{2}] \quad (16)$$

where U_t is an efficiency factor of 1.0 for symmetrical blocks, A_n is the net area in tension (Clause 12), and A_{gv} is the gross area in shear. Assuming the initial steel is 260W ($F_u = 410$ MPa, $F_y = 260$ MPa) and the critical fracture pattern shown below in Figure A.4:

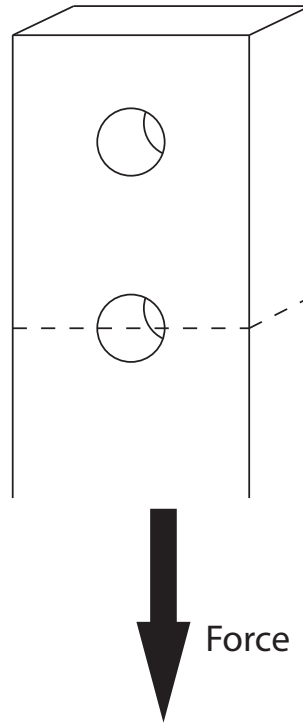
Net Section Fracture

Figure A.2: Net section connection fracture

$$T_r = (1.0)(12.7 \text{ mm})(44 - 14.7 \text{ mm})(410 \text{ MPa})$$

$$T_r = 153 \text{ kN}$$

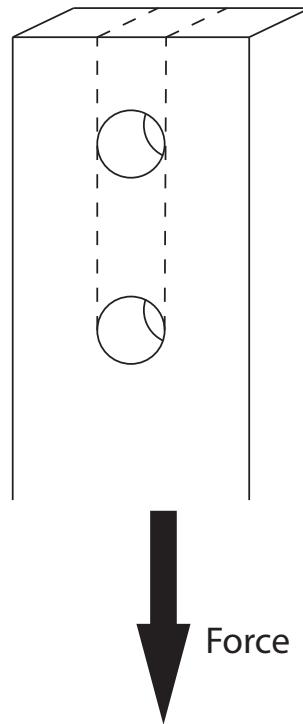
Bolt Tear Out

Figure A.3: Bolt tear out connection fracture

Assuming the adapter is made from 300W steel ($F_u = 410$ MPa, $F_y = 260$ MPa):

$$T_r = [0.6(12.7 \text{ mm} * (22 + 35 \text{ mm}) * 2 \text{ sides})\left(\frac{410 \text{ MPa} + 260 \text{ MPa}}{2}\right)]$$

$$T_r = 291 \text{ kN}$$

Bolt Bearing

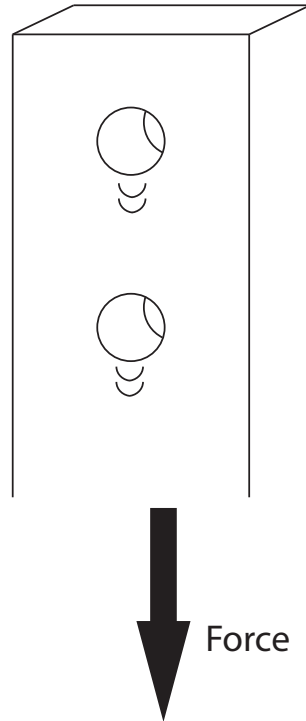


Figure A.4: Bolt bearing connection fracture

$$T_r = (3)(2 \text{ holes})(12.7 \text{ mm})(12.7 \text{ mm})(410 \text{ MPa})$$

$$T_r = 397 \text{ kN}$$

As shown through these calculations, the connection ends of the steel yielding core will withstand the 45 kN design forces for this study.

B SHIMADZU ADAPTER DESIGN

As seen from Figure 3.4, the adapter that was required to be attached to the Shimadzu in order for the specimens to be tested had three components. The bottom component is designed to withstand only compression forces, the top component only experiences tension, while the middle component was designed to withstand both depending on the loading phase. Based on the steel coupons tested in the first batch of device specimens, the peak coupon force was close to 180 kN. A baseline for the adapters was to remain elastic until 200 kN.

In all cases, the connection ends of the adapter as shown in Figure B.1 were oversized to remain elastic to greater than 1000 kN as shown below. Figures B.4, B.3, and ?? show the critical failure modes that were examined. The engineering drawings for each section of the adapter can be found at the end of this appendix.

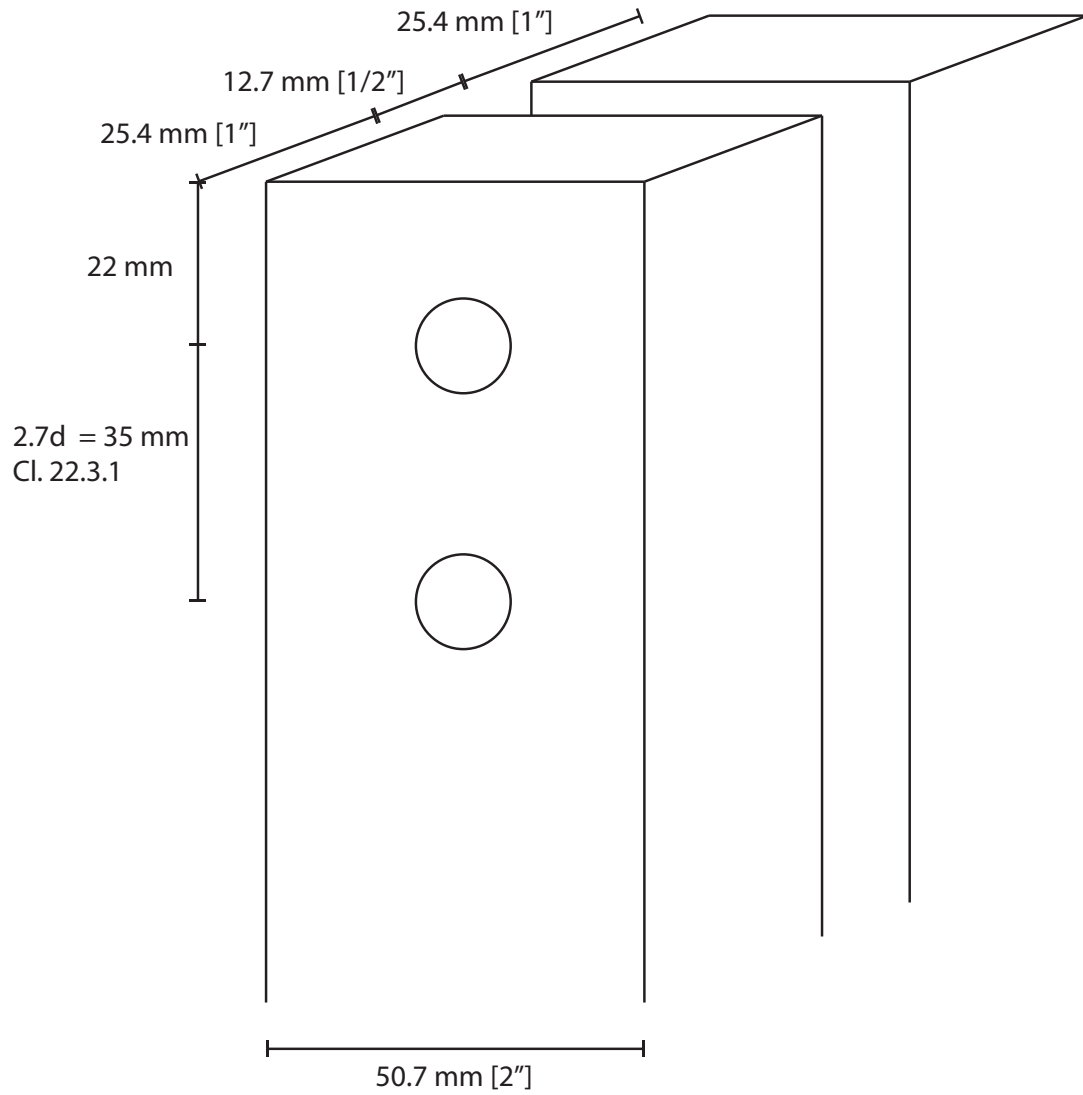


Figure B.1: Adapter connections

Net Section Fracture

$$T_r = (1.0)(25.4 \text{ mm})(50.7 - 14.7 \text{ mm})(440 \text{ MPa}) * 2 \text{ plates}$$

$$T_r = 805 \text{ kN}$$

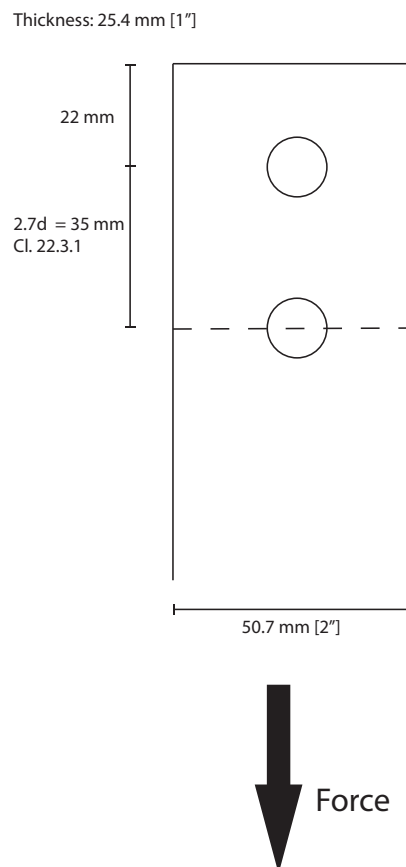


Figure B.2: Adapter net fracture

Bolt Tear Out

Assuming the adapter is made from 300W steel ($F_u = 440$ MPa, $F_y = 300$ MPa):

$$T_r = [0.6(25.4 \text{ mm} * (22 + 35 \text{ mm}) * 2 \text{ plates} * 2 \text{ sides}) \left(\frac{440 \text{ MPa} + 300 \text{ MPa}}{2} \right)]$$

$$T_r = 1285 \text{ kN}$$

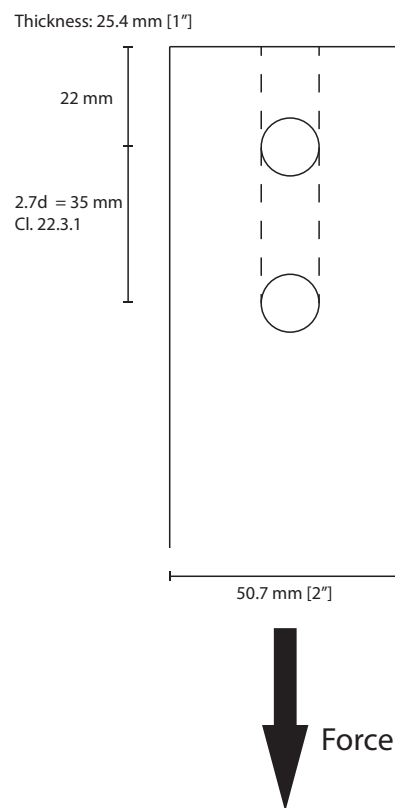


Figure B.3: Adapter bolt tear out

Bolt Bearing

$$T_r = (3)(2 \text{ holes})(12.7 \text{ mm})(25.4 \text{ mm})(440 \text{ MPa}) * 2 \text{ plates}$$

$$T_r = 1703 \text{ kN}$$

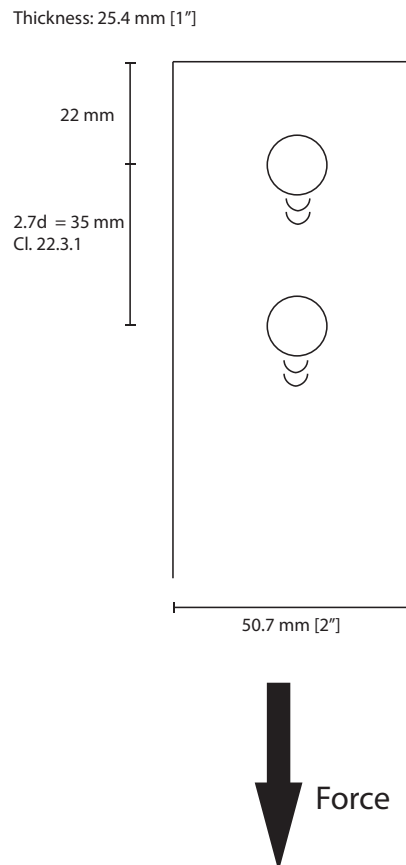
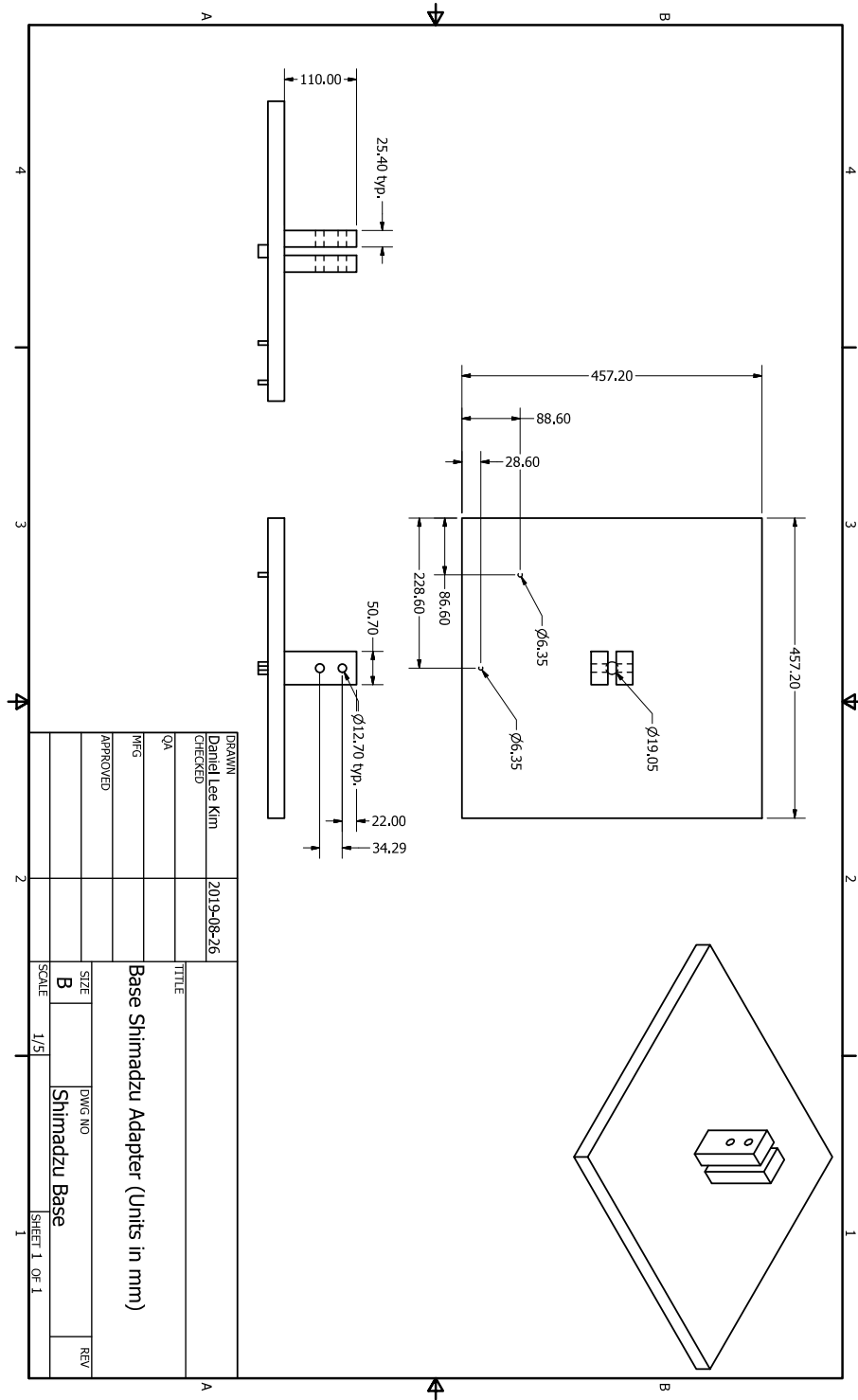
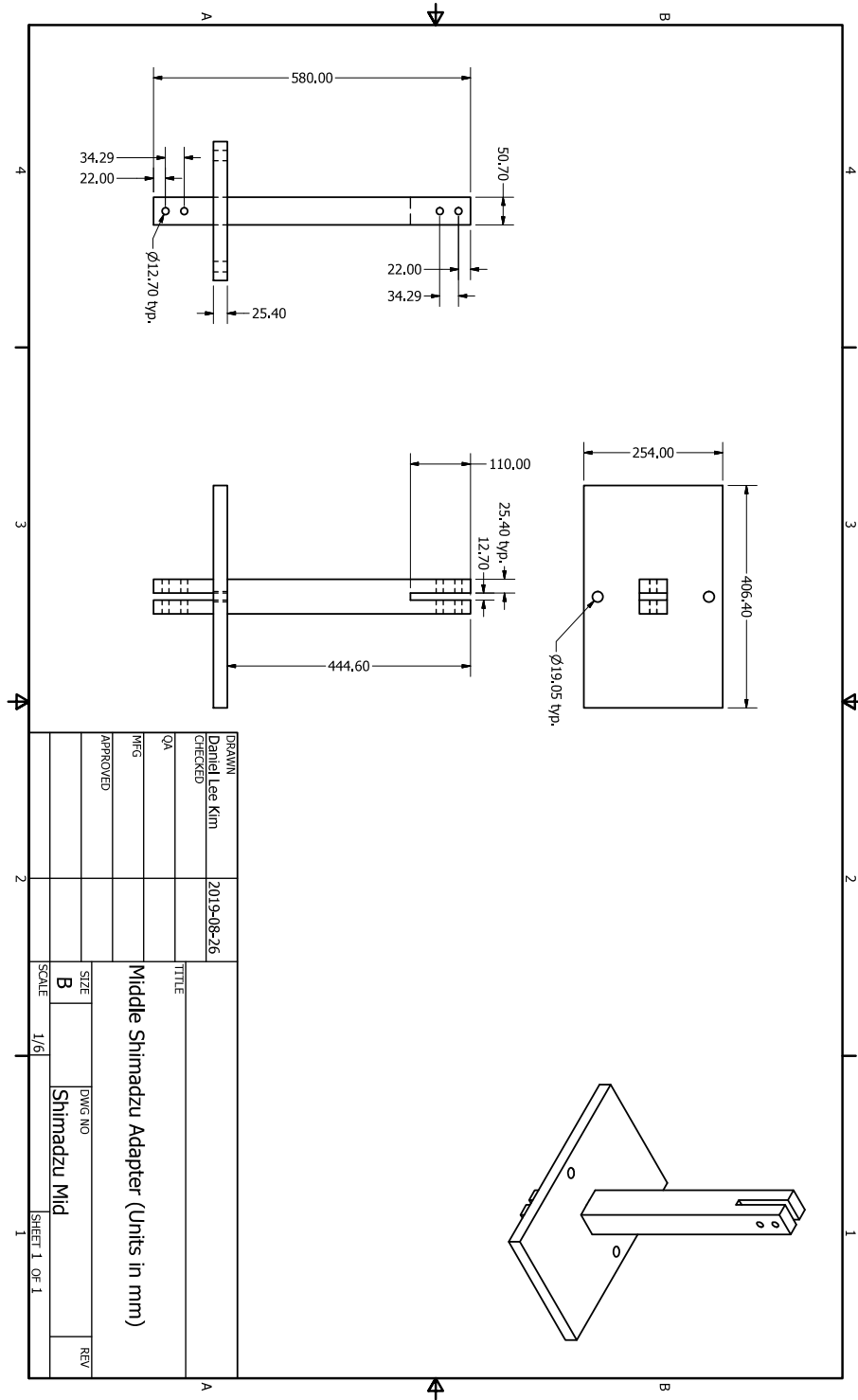


Figure B.4: Adapter bolt bearing failure





C APPENDIX REFERENCES

CISC (Canadian Institute of Steel Construction). 2014. Commentary on CSA Standard S16-14 Design of steel structures. Mississauga, ON.